View metadata, citation and similar papers at core.ac.uk

brought to you by CORE

provided by Digital Repository @ Iowa State University

IOWA STATE UNIVERSITY
Digital Repository

Retrospective Theses and Dissertations

Iowa State University Capstones, Theses and Dissertations

1960

Measurement of the mean square vibration amplitudes of atoms in metals by x-ray techniques

Earle Richard Ryba
Iowa State University

Follow this and additional works at: https://lib.dr.iastate.edu/rtd

 Part of the Condensed Matter Physics Commons

Recommended Citation
Ryba, Earle Richard, "Measurement of the mean square vibration amplitudes of atoms in metals by x-ray techniques " (1960). *Retrospective Theses and Dissertations*. 2391.
https://lib.dr.iastate.edu/rtd/2391

This Dissertation is brought to you for free and open access by the Iowa State University Capstones, Theses and Dissertations at Iowa State University Digital Repository. It has been accepted for inclusion in Retrospective Theses and Dissertations by an authorized administrator of Iowa State University Digital Repository. For more information, please contact digirep@iastate.edu.

This dissertation
has been microfilmed
exactly as received

Mic 61-470

RYBA, Earle Richard. MEASUREMENT OF THE MEAN SQUARE VIBRATION AMPLITUDES OF ATOMS IN METALS BY X-RAY TECHNIQUES.

Iowa State University of Science and Technology
Ph.D., 1960
Physics, solid state

University Microfilms, Inc., Ann Arbor, Michigan

MEASUREMENT OF THE MEAN SQUARE VIBRATION AMPLITUDES OF ATOMS IN METALS BY X-RAY TECHNIQUES

by

Earle Richard Ryba

A Dissertation Submitted to the
Graduate Faculty in Partial Fulfillment of
The Requirements for the Degree of
DOCTOR OF PHILOSOPHY

Major Subject: Metallurgy

Approved:

Signature was redacted for privacy.

In Charge of Major Work

Signature was redacted for privacy.

Head of Major Department

Signature was redacted for privacy.

Dean of Graduate College

Iowa State University
Of Science and Technology
Ames, Iowa

1960

TABLE OF CONTENTS

I. INTRODUCTION

A. The Temperature Effect

In the diffraction of x-rays by crystals the atoms arranged in a regular three-dimensional array act as scatterers which produce reflected beams in accordance with Bragg's law. The intensity of the reflected beam depends upon, apart from experimental factors, the scattering power of the individual atoms and the coherence of the scattering between the separate atoms. If, however, this three-dimensional array is disturbed in some fashion, as it is when the atoms in the crystal lattice vibrate in thermal motion, the coherence of scattering is partially destroyed, and a reduction in the intensity of the reflected beam results. The intensity of the reflected beam is more reduced the greater the distance the atom moves away from its equilibrium rest position. Thus, the reduction in the intensity of the Bragg reflection becomes a measure of the vibration amplitudes of the atoms.

The energy lost in the reduction of the intensity of the Bragg reflection reappears as a diffuse scattering. Early diffraction theory regarded this diffuse scattering as a broad maximum of general scattering at moderate angles. Subsequent theory, in which the atoms were not considered to vibrate independently but rather in a cooperative fashion as in the Debye theory of lattice vibrations, showed that the thermal diffuse scattering appears as diffuse maxima in the vicinity of the Bragg reflections. Diffraction experiments have verified that

this is the correct description.

The theory concerning these two aspects of the temperature effect in x-ray diffraction is discussed in detail in James (1), chapters I and V. A brief outline of the theoretical results will be presented here in order to show that an experimental investigation of the temperature effect gives a quantitative measure of the mean square vibration amplitude of atoms in crystals.

B. The Amplitude of Vibration

In the case where the atoms in a monatomic crystal lattice are considered to be independently-vibrating harmonic oscillators, it can be shown that:

$$\bar{J} = \frac{\phi_o^2}{R^2} N(1 - e^{-2M}) + e^{-2M} J_o, \qquad (1)$$

where:

$$2M = \Gamma^2 \mu^2, \qquad (2)$$

$$\Gamma = \frac{4\pi \sin \theta}{\lambda}. \qquad (3)$$

$\bar{J}$ is the average reflected intensity, ϕ_o is the amplitude of a reflected wave, R is the distance between the sample and the point of observation, N is the number of scatterers, J_o is the intensity of reflection from a rest lattice, θ is the Bragg angle, λ is the radiation wavelength, and μ^2 is the mean square vibration amplitude of the atoms in a direction normal to the lattice planes in question. The first term in equation 1 represents the thermal diffuse scattering as a broad diffuse

maximum, and the second term represents the intensity of the Bragg reflection from a rest lattice reduced by the temperature factor e^{-2M}.

In the second theoretical approach, the true motion of the atoms in the lattice is more closely approximated by considering them to be vibrating as coupled harmonic oscillators which result in plane standing waves in the lattice. The displacement of any atom can then be represented as a sum of sine or cosine terms for each lattice wave. The resulting equation for the reflection intensity in the reciprocal lattice direction $\underset{\sim}{s}/\lambda$ is:

$$\bar{J}\,(\underset{\sim}{s}/\lambda) = \left|f_o\right|^2 e^{-2M} J_o\,(\underset{\sim}{s}/\lambda) + J_2\,(\underset{\sim}{s}/\lambda). \qquad (4)$$

$\bar{J}$ is the average reflected intensity, f_o is the atomic scattering factor. J_o is the reflection intensity from a rest lattice, and $J_2\,(\underset{\sim}{s}/\lambda)$ represents an intensity term having broad diffuse maxima in the direction of the Bragg reflections. The first term in equation 4 represents the reduction in the intensity of the Bragg reflection from a rest lattice by the factor e^{-2M}. Thus, both treatments give the same form for the temperature factor, and differ in the form of the intensity term for the thermal diffuse scattering.

The thermal diffuse scattering exhibits a maximum at the position of the Bragg reflection peak, which is small compared to the intensity of the Bragg reflection. However, the contribution of the thermal diffuse scattering to the intensity of the Bragg reflection becomes more significant for crystals of substances with low Debye temperatures. This contribution also becomes greater for the higher-angle reflections.

Therefore, several methods have been offered in the literature to correct the intensity of a Bragg reflection for the contribution of the thermal diffuse scattering. Nilson (2) has proposed an analytical technique which requires a knowledge of the intensity of the thermal diffuse scattering near the Bragg reflection. Young (3) has suggested, since theory indicates that the contribution of the thermal diffuse scattering to the intensity of the Bragg reflection approaches zero at $\sin \theta = 0$, that a plot of the temperature factor versus $\left(\frac{\sin \theta}{\lambda}\right)^2$ will yield an M value free of error due to the thermal diffuse scattering at $\sin \theta = 0$. However, neither of these methods is as yet well developed, and the contribution of the thermal diffuse scattering is often neglected in making intensity measurements.

If the intensity term for the diffuse scattering is neglected, it can be shown from equations 2 and 4 that:

$$\ln \frac{R(T_2)}{R(T_1)} = \Gamma^2 \left[\mu^2(T_1) - \mu^2(T_2) \right] , \qquad (5)$$

where R is the integrated intensity of reflection. From this expression, it appears that only differences in the mean square vibration amplitudes can be determined from measurements of reflection intensity at various temperatures. However, an absolute value of the mean square vibration amplitude can be determined from these measurements with the aid of the following theoretical evaluation of the quantity M. The crystal is assumed to be an isotropic, continuous solid, and the Debye method can be applied. Then:

$$M = \frac{3h^2}{2mk\Theta_M} \Gamma^2 \left[\frac{\phi(x)}{x} + \frac{1}{4} \right], \qquad (6)$$

where:

$$\phi(x) = \frac{1}{x} \int_0^x \frac{\xi \, d\xi}{e^{\xi} - 1} , \tag{7}$$

$$x = \frac{\hbar \omega_{max}}{kT} , \tag{8}$$

$$\xi = \frac{\hbar \omega}{kT} . \tag{9}$$

h = Planck's constant, m is the mass of the atom, k is Boltzmann's constant, and Θ_M is the mean Debye temperature. Thus, from equations 2 and 6:

$$\mu^2 = \frac{3\hbar^2 T}{mk\Theta_M^2} \left[\phi(x) + \frac{1}{4} \right] . \tag{10}$$

This expression can be evaluated from Debye temperatures and values of $\phi(x)$ tabulated in, for example, Internationale Tabellen zur Bestimmung von Kristallstrukturen (4). Alternatively, an expansion of the integral can be made for $T > \Theta/2\pi$. The resulting expression is:

$$\mu^2(T) = \beta T + \gamma T^{-1} + \delta T^{-3} + \ldots , \tag{11}$$

where:

$$\beta = \frac{3\hbar^2}{mk\Theta_M^2} , \tag{12}$$

$$\gamma = \frac{\hbar^2}{12mk} , \tag{13}$$

$$\delta = \frac{-\hbar^2 \Theta_M^2}{1200mk} . \tag{14}$$

To use intensity measurements of a reflection at various temperatures to calculate μ^2, equations 5 and 11 can be combined to give:

$$\ln \frac{R(T_2)}{R(T_1)} = \Gamma^2 \left[\beta(T_1 - T_2) + \gamma(T_1^{-1} - T_2^{-1}) + \delta(T_1^{-3} - T_2^{-3})\right] . \quad (15)$$

Then, β can be determined from this equation, since γ can be calculated and δ, being contained in a very small term, can be approximated by using a Debye temperature from some other type of measurement. The substitution of this measured β into equation 11 gives the required mean square amplitude function.

C. The Debye Temperature

Another quantity that can be derived from equation 15, with the aid of equation 12, is the mean Debye temperature Θ_M. The Debye temperature is of interest because many macroscopic properties of solids can be expressed as a function of Θ/T. It should be pointed out, however, that the mean Debye temperature determined in this way from x-ray measurements is always a few per cent larger than the Debye temperature determined from other methods. This is due to the manner in which the Debye temperatures for the longitudinal and transverse waves are averaged. For the Debye temperature Θ_D:

$$3\Theta_D^{-3} = \Theta_l^{-3} + 2\Theta_t^{-3} , \quad (16)$$

whereas for the mean Debye temperature obtained from x-ray measurements:

$$3\Theta_M^{-2} = \Theta_l^{-2} + 2\Theta_t^{-2} , \quad (17)$$

as can be seen from equation 10.

It should be pointed out that one of the assumptions made in deriving equations 6-15, given in the previous section, is that the volume remains constant as the temperature of the crystal is changed. It is possible to correct for this assumption by considering the Debye temperature to be a function of temperature. Zener and Bilinsky (5) have shown that it is possible to calculate the Debye temperature at any temperature if the enthalpy of the substance in question is known at that temperature. Owen and Williams (6) and Paskin (7) have derived the relation:

$$\theta(T) = \theta(T_o) \left(\frac{V(T_o)}{V(T)} \right)^{\gamma} \qquad (18)$$

which related the change of the Debye temperature with temperature to the thermal expansion. In equation 18, V is the volume and γ is the temperature-independent Grüneisen constant. This correction is easier to apply than that of Zener and Bilinsky since thermal expansion data are readily available. Paskin also shows that when the quantity log $R(T)/R(T_o)$, obtained from a set of intensity measurements at various temperatures, is plotted against a reduced temperature defined as:

$$T' = T \left(\frac{V(T)}{V(T_o)} \right)^{2\gamma}, \qquad (19)$$

the data fit the straight line predicted for high temperatures by equation 15 quite well.

D. Previous Experimental Work

Determinations of μ^2 and θ_M through the use of the above equations have been made for the metals copper, aluminum, gold, silver, and titanium. James, Brindley, and Wood (8) studied large single crystals of aluminum at 290°K and 86°K, using an ionization chamber x-ray spectrometer. They reported their results in the form of equation 11, and also as a Debye temperature for the temperature range studied. Owen and Williams (6) studied powder samples of copper, gold, and aluminum, using a Debye-Scherrer camera constructed for use at temperatures between room temperature and 600°C. They found that the function formed by the differences of the M values of equation 6 fit the data very well when plotted as ln $R(T)/R(T_o)$ versus temperature, if the Debye temperature is corrected for thermal expansion. In the case of the aluminum measurements, this fit was very good only up to 600°K. The scatter in the data for copper, for example, is approximately $\pm$ 8% from the best curve through the data. Debye temperatures were calculated from the results for the three metals for temperatures from 100°K to 900°K; their Debye temperature for aluminum at 190°K agrees exactly with the value reported by James, Brindley, and Wood. Boskovits, et al. (9) examined silver wires at temperatures from 81° to 774°K, using a counter goniometer fitted with a cryostat and a device for blowing hot air onto the sample. Debye temperatures were reported for this temperature range. The intensity values between runs varied about $\pm$ 7% from the mean intensity value at a particular temperature. Spreadborough and Christian (10) studied polycrystalline samples of silver from room temperature to the melting

point and polycrystalline samples of titanium from room temperature to about 1080°C, using a high temperature x-ray diffractometer. Their results on silver, when plotted against the reduced temperature defined by equation 19, gave the appropriate straight line, and a Debye temperature which disagrees with the value obtained by Boskovits, et al., at room temperature. The results on titanium were not given, except for an approximate Debye temperature calculated according to equation 15, neglecting the last two terms.

E. Formulation of the Problem

The main objective of this investigation was to determine the mean square vibration amplitude as a function of temperature for copper and zinc from the change with temperature of the integrated intensity of a Bragg reflection. Several reflections from large single crystals of these metals were examined from temperatures of 13°C to a temperature close to the melting point of the metal being examined. The results of the measurements on the copper single crystal can be compared to the results of Owen and Williams and to the values predicted by equation 15. The measurements on the zinc single crystals can be used to examine the anisotropy of the thermal vibrations in this metal by examining the reflections which give the mean square vibration amplitudes along the c and a axes. For both metals Debye temperatures can be calculated as a function of temperature from equation 15.

In the theory of electrical resistivity, the resistance to the motion of the electrons through the metal lattice is considered to arise

from the scattering of the electrons by imperfections in the lattice. These imperfections are mainly the motion of the atoms away from their rest positions in the lattice. Mott and Jones (11), page 244, have shown, then, that the electrical resistivity is directly proportional to the mean square vibration amplitude of the atoms in the metal:

$$\rho(T) = C\mu^2(T). \tag{20}$$

Values of the electrical resistivity and the experimental values of the mean square vibration amplitude can be used to evaluate the proportionality constant C, and to determine the temperature range over which equation 20 is valid. Also, the resulting values of C can be compared with the values calculated from the equation:

$$C = \frac{4(2mE_F)^{3/2}\,\bar{Q}_s}{3h^2e^2}, \tag{21}$$

which results from a theoretical derivation given in Appendix A. This derivation utilizes the classical Einstein model and therefore is valid only for $T > \theta$.

It was shown previously from equation 5 that only differences in the mean square vibration amplitude can be determined from x-ray intensity measurements at different temperatures if the Debye evaluation of the quantity M is not employed. In order to obtain the desired mean square vibration amplitude function from the intensity measurements, an approximation of $\mu^2(T_1)$ can be made, and thus a scaled function of the mean square amplitude can be derived as follows. An expanded form of equation 4, neglecting the thermal diffuse scattering, is:

$$R_{hkl}(T) = KR'_{hkl}(T) = \left| F_{hkl} \right|^2 e^{-\Gamma^2 \mu^2_{hkl}(T)} , \qquad (22)$$

where $R_{hkl}(T)$ is the scaled value of the integrated intensity of the reflection (hkl), in arbitrary units, at the temperature T, $R'_{hkl}(T)$ is the observed value, F_{hkl} is the structure factor for the reflection (hkl), and K is the scaling factor. Equation 22 can be solved for K, using the experimental value of $R_{hkl}(T_o)$ and a value of $\mu^2_{hkl}(T_o)$ calculated from equation 11, or the equation:

$$\mu^2(T) = \frac{3\hbar^2 T}{mk\Theta_M^2} , \qquad (23)$$

using an appropriate Debye temperature. All the data can then be scaled by multiplying by K, and the function $\ln R_{hkl}(T)$ can be developed and substituted into the equation:

$$\mu^2_{hkl}(T) = \Gamma^{-2} \left[\ln \left| F_{hkl} \right|^2 - \ln R_{hkl}(T) \right], \qquad (24)$$

which is derived from equation 22. The desired function $\mu^2_{hkl}(T)$ results. Note here that none of the ordinary corrections to the intensity, such as the absorption, Lorentz, polarization, etc. corrections, have to be made to obtain the mean square vibration amplitude function.

The function $\ln R_{hkl}(T)$ will be expressed as an equation of the form:

$$\ln R_{hkl}(T) = \sum_{n=0}^{3} a_n T^n \qquad (25)$$

This expansion of $\ln R_{hkl}(T)$ appeared to be the most suitable because powers of T result for the mean square amplitude function when

equations 24 and 18 are combined and the dependence of the volume on temperature is expressed in the form:

$$V(T) = b_o + b_1 T \,, \tag{26}$$

γ being approximately equal to 2 for metals.

The calculations for fitting the function in equation 25 were performed on an International Business Machines Type 650 computer. A program for scaling the intensity data, making the fit, and performing the necessary calculations to obtain equation 24 is described in Appendix B. Also described therein are programs for fitting an analytical function to the data for the change in the interplanar spacing with temperature, and for calculating Debye temperatures as a function of temperature from equation 15.

II. EXPERIMENTAL

A. Apparatus

The apparatus employed in this investigation consisted of: 1) a Norelco water-cooled x-ray diffraction unit; 2) a Norelco diffractometer, outfitted with a high temperature chamber designed by Chiotti (12); 3) a means for evacuating the chamber, and pressurizing it with helium; 4) a power supply for heating the furnace; and 5) associated electronic measuring equipment.

A diagram of the high temperature chamber is shown in Figure 1. It consists of a water-cooled cover and a water-cooled backplate fixed to a hollow shaft which is inserted into the Norelco diffractometer, through which the chamber can be evacuated or pressurized. Mounted on the backplate are the furnace supports and heater lead terminals. The sample is supported by a tantalum bar, also mounted on the backplate, which could be rotated so that the surface of the sample coincides with the rotation axis of the diffractometer. The cover is bolted to the backplate and seals the chamber with a rubber "o" ring. Incident and reflected x-radiation pass in and out of the chamber through a 10 mil sheet of beryllium fixed to the chamber cover with an epoxy resin cement (Armstrong Adhesive A-6).

A diagram of the furnace used with this chamber is shown in Figure 2. The reflector shields were constructed of 5 mil tantalum sheet. The furnace was supported on the backplate so that the sample holder bar was positioned inside the heater element. The furnace

Figure 1. High temperature chamber for x-ray diffractometer

1. Chamber cover
2. Chamber backplate
3. Hollow mounting shaft
4. Sample holder bar
5. Sample rocker adjustment
6. Furnace mounts
7. Thermocouple
8. Beryllium window

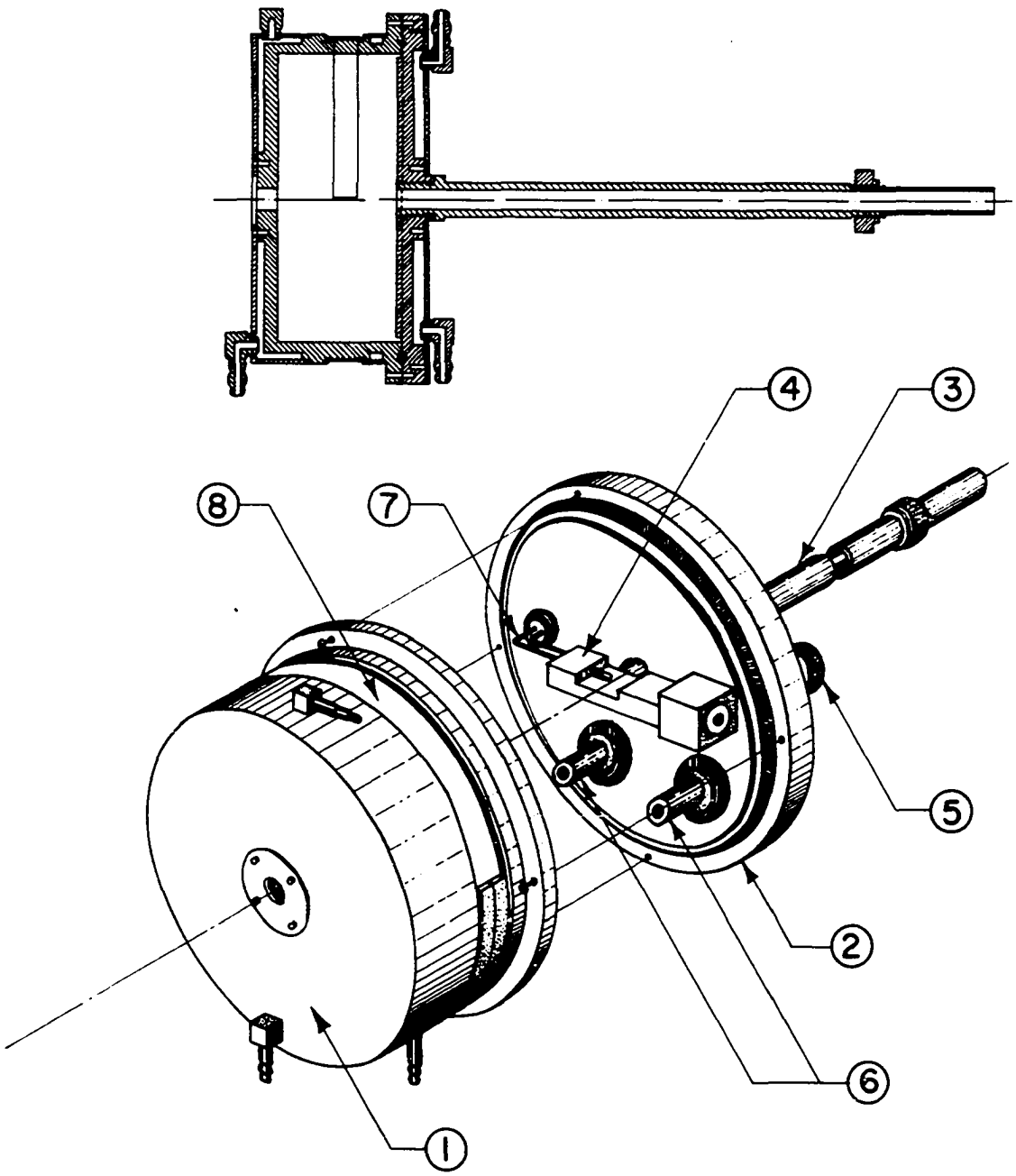
4
3
8
7
5
2
6
1

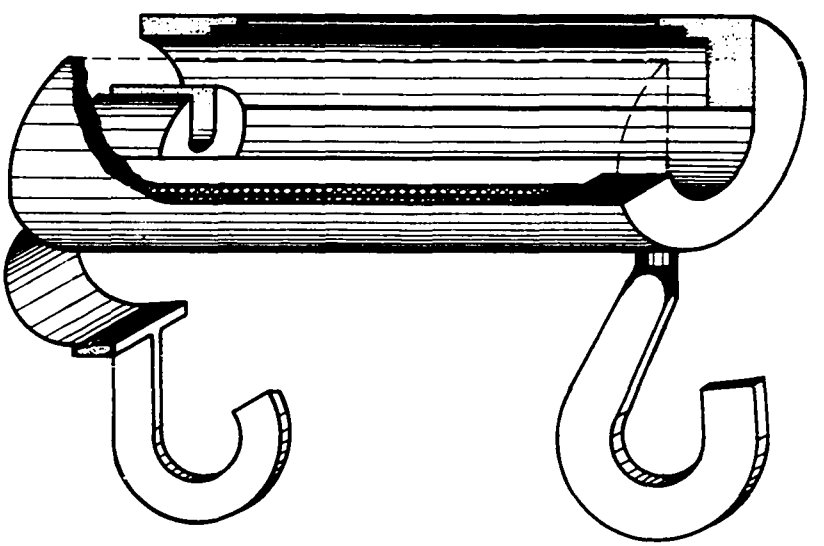

Figure 2. Furnace for high temperature chamber

power supply consisted of a 230 volt powerstat and a water-cooled, 10 KVA, 12-to-one stepdown transformer, which supplied current to the furnace through flexible stranded welding cables. A platinum-13% rhodium in platinum thermocouple was used to measure the temperature of the sample and was placed directly under the sample at one end. The temperature was read on a Rubicon potentiometer.

The chamber was evacuated with a fore pump through the hollow shaft on the backplate. Bottled helium, after being passed through a tube furnace containing zirconium metal turnings maintained at about 800°C, and a liquid nitrogen cold trap, could also be introduced through this shaft and out through a bubbler.

A block diagram of the electronic measuring equipment is shown in Figure 3. The output from a Norelco proportional counter mounted on the diffractometer was passed through its associated preamplifier, through another linear amplifier of Norelco design, and finally into a Norelco scaler-ratemeter and recorder unit.

Copper radiation was used in this investigation. The x-ray tube voltage was stabilized to 0.25% by the Norelco stabilized power supply. The tube filament current was stabilized to $\pm$0.1% by a Norelco current stabilizer mounted in the x-ray diffraction unit.

B. Materials

The two metals studied in this investigation were copper and zinc. The copper used 99.985% Cuprovac-E high purity copper, manufactured by Vacuum Metals Corporation. The zinc used was 99.9975% Special High

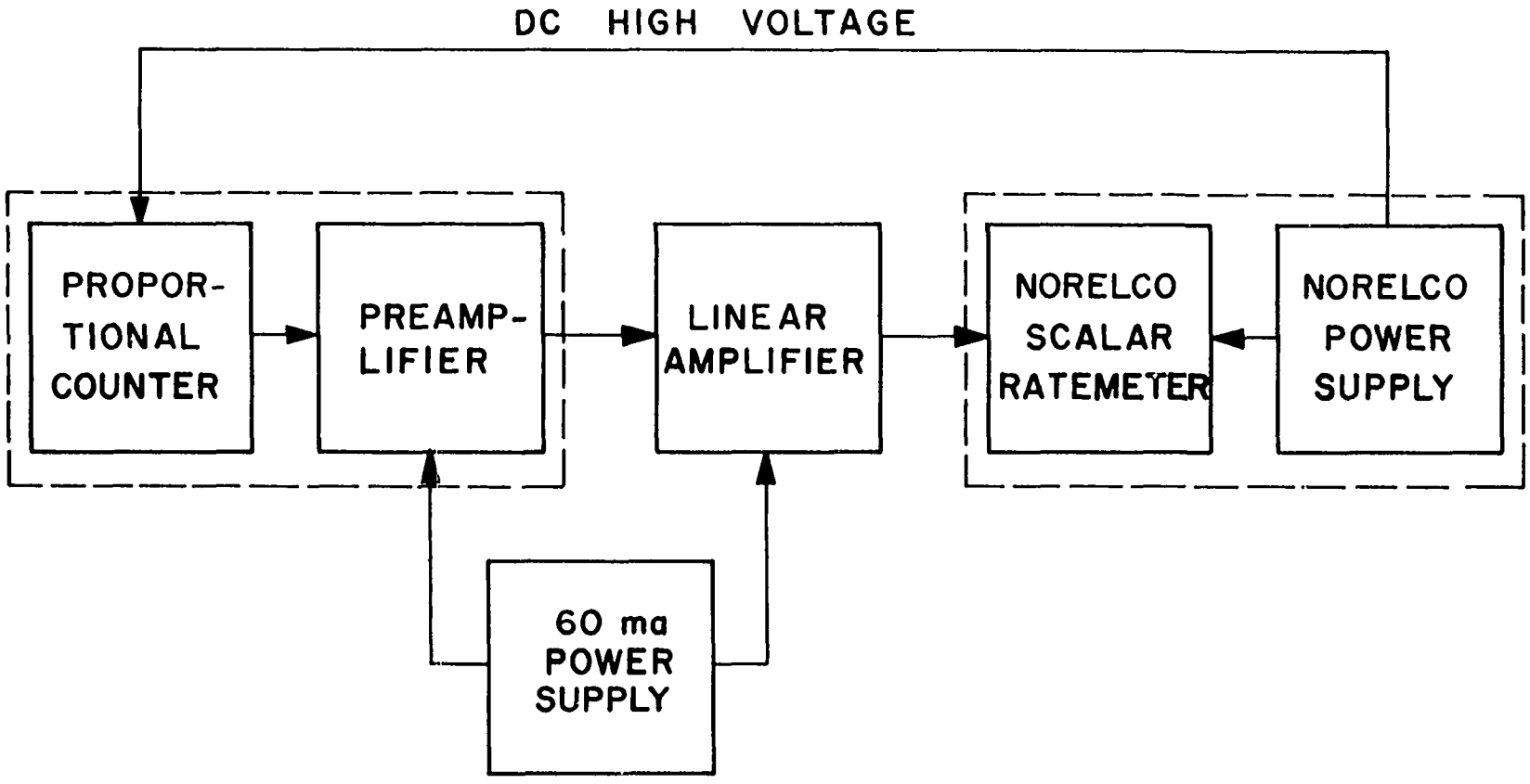

Figure 3. Block diagram of electronic measuring system

Grade electrolytic zinc, manufactured by The Bunker Hill Company.

The type of sample used in this work was a single crystal section with its section face cut perpendicular to a particular crystallographic direction. The directions chosen were [100] for copper, and [0001] and $[10\bar{1}0]$ for zinc. The results of the intensity measurements will then give the mean square vibration amplitudes along the a axis in copper and along the c and a axes in zinc. The crystal sections were 10 mm. x 25 mm. x 1.5 mm. in size.

Single crystals of copper and zinc were produced by melting pieces of the metals in a magnesium oxide crucible under vacuum, and then allowing the melt to cool slowly in a small temperature gradient. The resulting crystals were cylindrical in shape and one inch in diameter. The orientations of the crystals were determined from back-reflection Laue x-ray photographs, and the crystals were then rotated with respect to the x-ray beam so that they could be marked for sectioning perpendicular to the designated crystallographic direction. The Laue pattern of the zinc crystal oriented along the hexagonal a axis was matched to a standard $(2\bar{1}\bar{1}0)$ stereographic projection to insure that the proper orientation had been obtained. The error in orientation of the sections was estimated to be less than 1°. The sections were cut with a jeweler's saw, and hand polished to a smooth surface. In the case of the zinc sections oriented with their faces perpendicular to the hexagonal c axis, smooth surfaces were obtained by cleaving the large crystals. The zinc crystal sections were chemically polished in a 3:1 solution of concentrated nitric acid in water to remove the worked metal and

obtain a bright, smooth surface. The copper crystal section was etched with nitric acid to remove quantities of work metal, and further electropolished to obtain a bright, smooth surface.

C. Experimental Procedure

The diffactometer used for this work was frequently realigned. The takeoff angle was adjusted to 3°, and a zero alignment was made with a zero alignment slit before the high temperature chamber was mounted. Then, for each crystal section mounted, the sample was rotated slightly to obtain the maximum intensity of the reflection to be examined by means of the fine adjustment on the diffactometer. The intensity of the reflected beam from these large single crystals was so great that absorbers had to be interposed between the crystal and the counter to avoid overloading the scalar-ratemeter unit and the proportional counter. The absorbers consisted of assortments of 0.5 mil tantalum and 0.35 mil nickel foils glued to an aluminum slit for rigidity.

The aligned crystal section was clamped to the sample holder bar with a small tantalum clamp. The furnace was mounted and the chamber assembled. The chamber was evacuated to approximately ten microns of mercury pressure, whereupon helium was introduced into the system. This procedure was repeated several times before a run was begun.

After calibration of the ratemeter, reflections were scanned and recorded, with the counter moving at a rate of $1/8^{\circ}$ 2θ per minute. For most runs, two peaks of the desired reflection were recorded at each temperature, both on heating and on cooling, at 100°C intervals between

13°C and the melting point of the metal being studied. The sample temperature was allowed to equilibrate before the peak was recorded. Temperature variations during the 10 to fifteen minutes recording time were less than 2°C for most of the peaks recorded.

The integrated intensities of the reflections were obtained by tracing the recorded peaks with a planimeter. In the reflections examined, the α_1 and α_2 peaks were not completely separated, so both peaks were used for the intensity measurement. The peaks were traced several times, assuming that they were smooth curves. Enough background trace was recorded on both sides of the peaks to determine the background level under the peak. No correction for thermal diffuse scattering was made in measuring the intensities, since it was felt that this contribution was small compared to the very large Bragg reflection intensities, and no change in shape of the background trace near the peak with temperature could be observed. The center of gravity of the α_1 peak at half-height was estimated to obtain the Bragg angle.

Tables 1 and 2 list the various runs made, the reflections examined, the temperature range investigated, and the manner in which the peaks were recorded for the copper and zinc single crystals respectively.

Table 1. Description of runs made on copper single crystal

Run No.	(hkℓ)	Temperature range
VIII	(400)	800°C → 13°C
XVa	(400)	800°C → 13°C
XVb	(400)	14°C → 1000°C → 14°C
XVc	(400)	14°C → 1000°C → 13°C

Table 2. Description of runs made on zinc single crystals

Run No.	(hkiℓ)	Temperature range
Xb	(0004)	13°C → 400°C
XII	(0006)	16°C → 400°C → 200°C
XIIIa	(0006)	400°C → 13°C → 200°C; 13°C → 400°C → 14°C
XIIIb	(0006)	14°C → 400°C → 14°C
XIV	(0004)	14°C → 400°C → 14°C
XVIII	(2$\bar{1}\bar{1}$0)	14°C → 400°C → 14°C → 400°C → 14°C → 400°C → 14°C

III. RESULTS AND DISCUSSION

A. Intensities and Mean Square Vibration Amplitudes

The observed intensity and Bragg angle data for the runs made on the copper single crystal are listed in Table 4 in Appendix C. Plots of the natural logarithm of the scaled intensities versus temperature for the four runs are shown in Figures 4 to 7. The intensities for the copper single crystal were scaled by calculating a mean square vibration amplitude for the lowest temperature of measurement from equation 11, using a Debye temperature of 315°K, and then calculating a scaling factor from equation 22. Also shown on these plots are the curves representing the least squares fit of equation 25 to the data. Most of the intensity values are within about ±2% of the least squares curve for runs VIII and XVa, and within ±3.5% for runs XVb and XVc.

The data of all four runs were scaled together, and these are plotted in Figure 8, along with the least squares fit of equation 25 to the combined data. Most of the intensity values are within ±6% of the least squares curve in this plot. The function $\ln R_{400}(T)$, in the form of equation 25, is:

$$\ln R_{400}(T) = 7.5347 - 5.8266 \cdot 10^{-4} T - 9.7793 \cdot 10^{-7} T^2 + 3.4911 \cdot 10^{-10} T^3, \qquad (27)$$

where T is in °C. Since the data points are grouped every 100°, a mean value of the intensity and a standard deviation were calculated for each

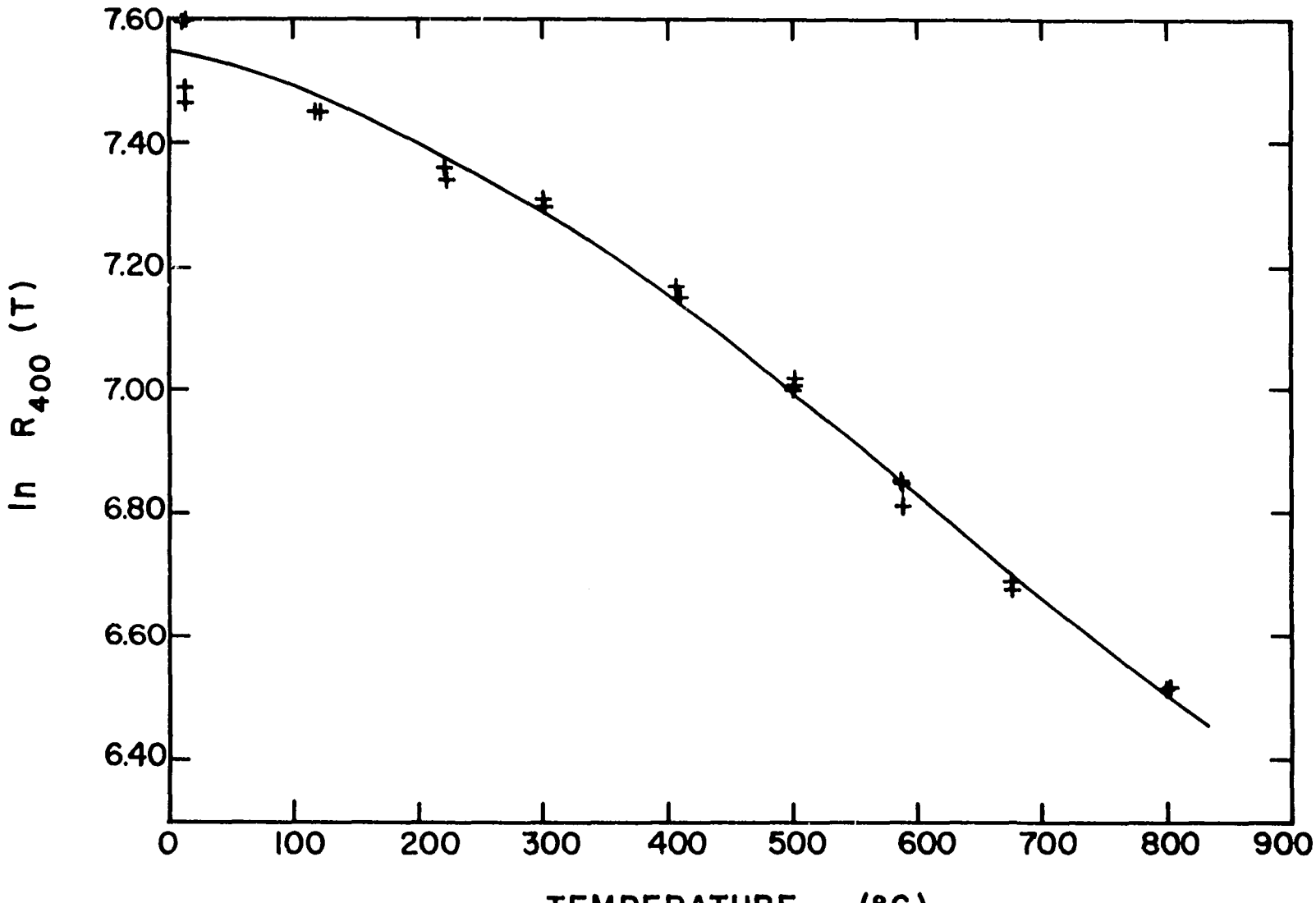

Figure 4. ln $R_{400}(T)$ versus temperature for copper. Run VIII

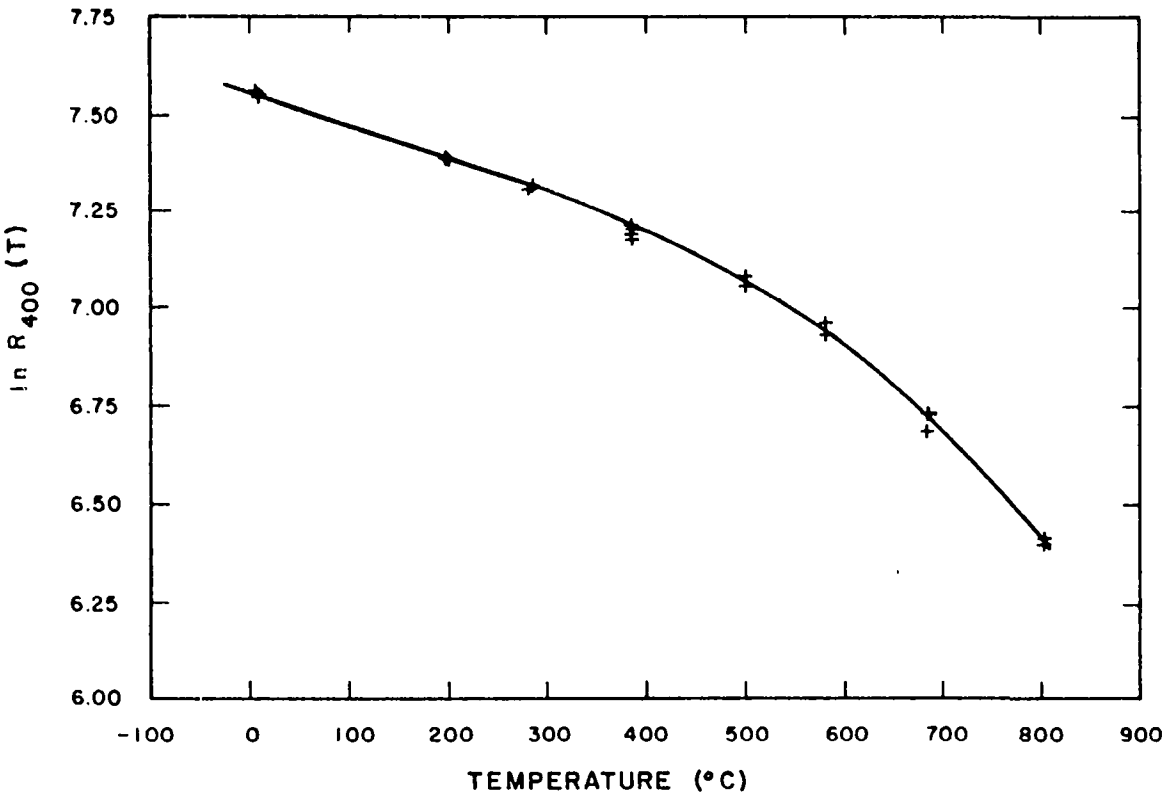

Figure 5. ln $R_{400}(T)$ versus temperature for copper. Run XVa

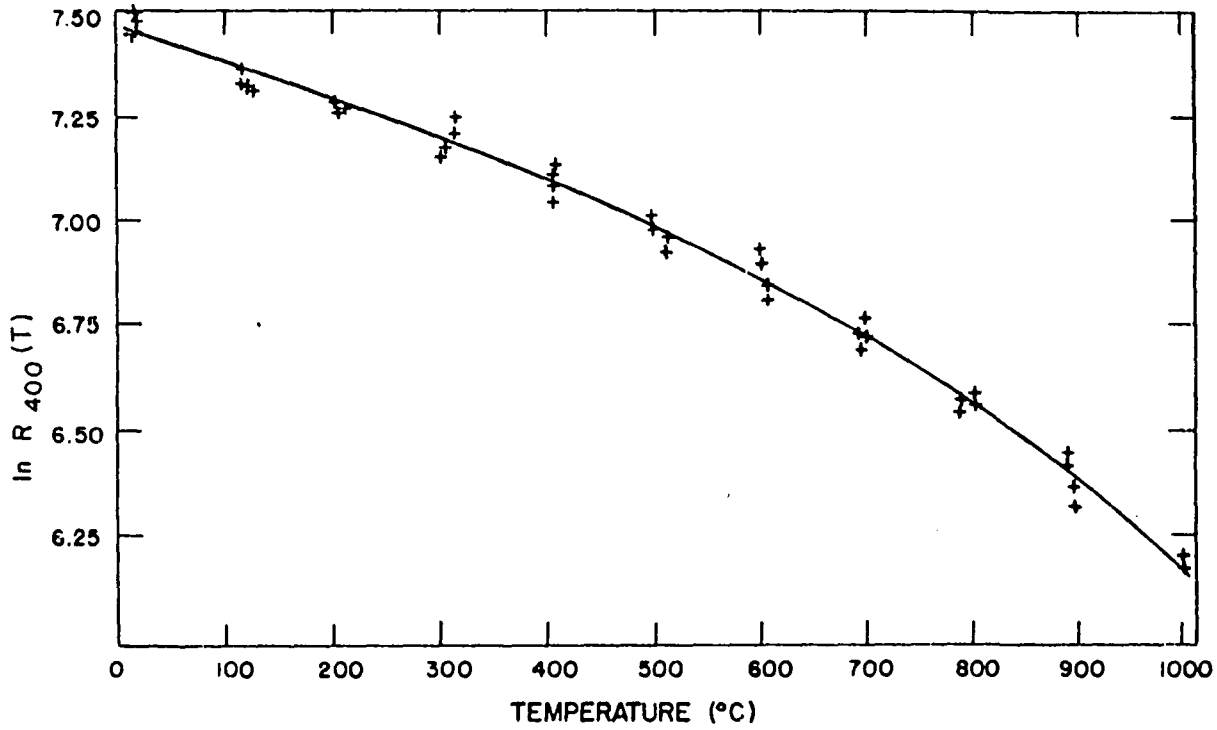

Figure 6. ln $R_{400}(T)$ versus temperature for copper. Run XVb

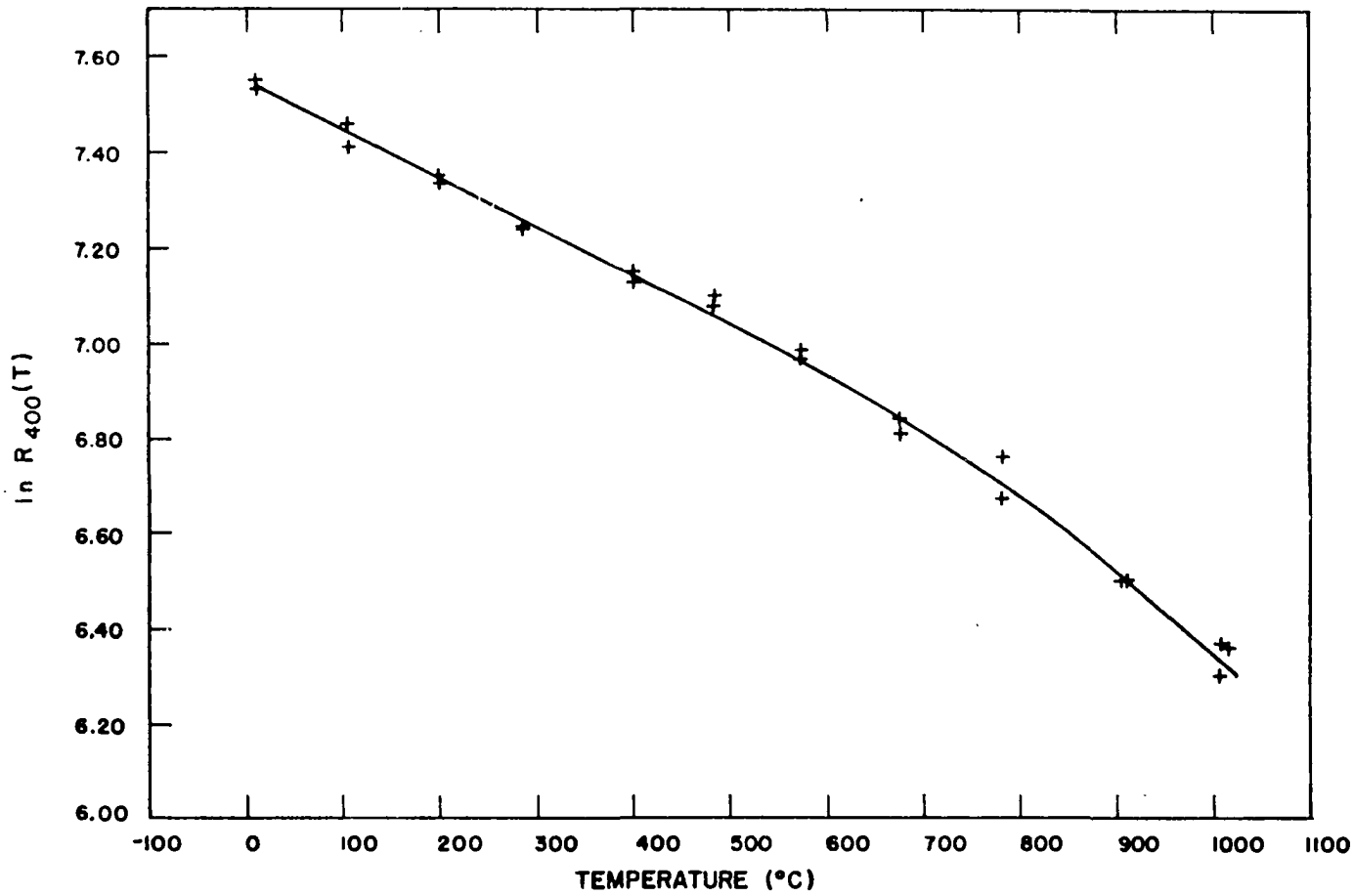

Figure 7. ln $R_{400}(T)$ versus temperature for copper. Run XVc

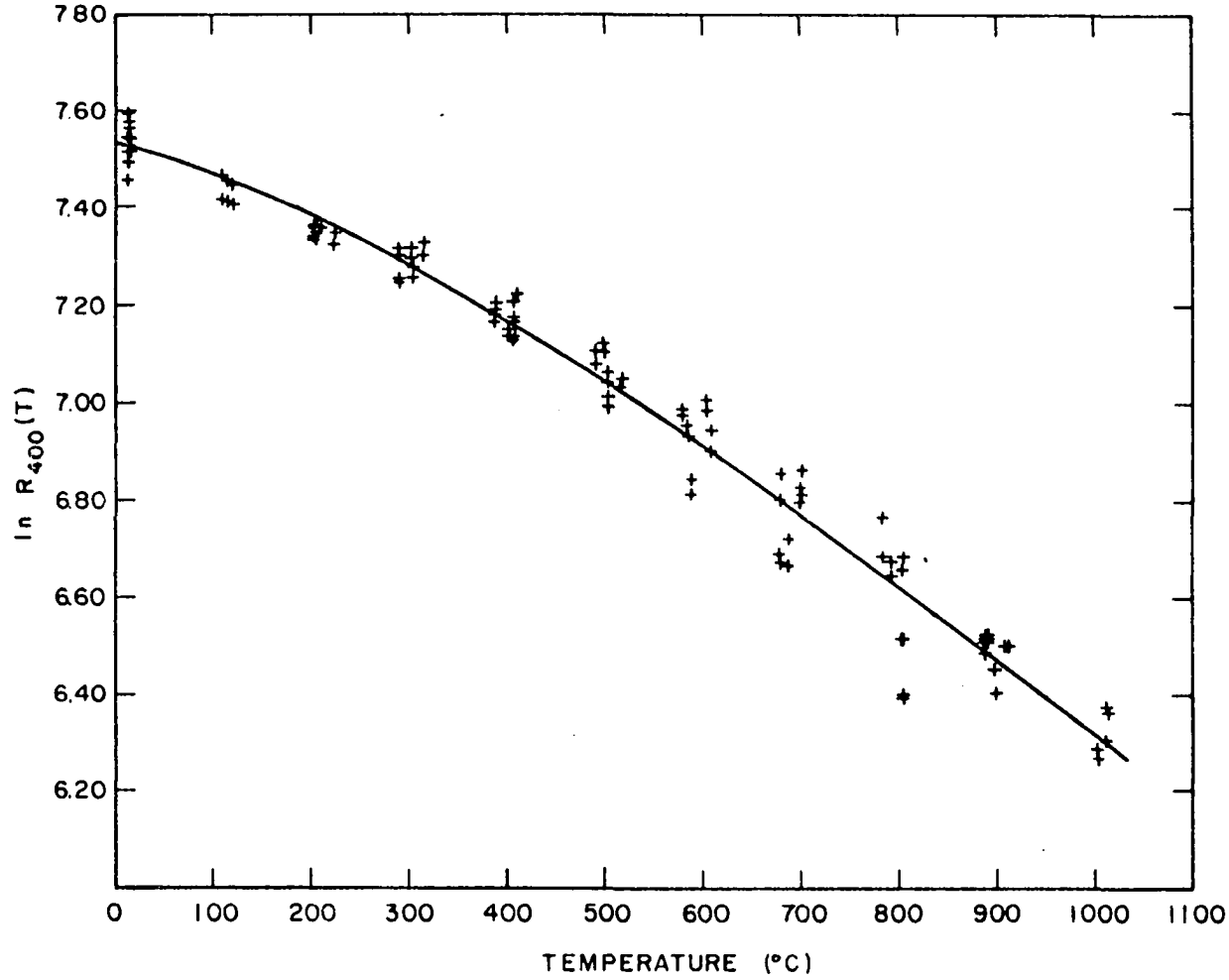

Figure 8. ln $R_{400}(T)$ versus temperature for copper. All runs

group of values. The main intensity values and the resulting standard deviations are indicated in Figure 9. The mean square amplitude of vibration as a function of temperature was calculated by substituting the function ln $R_{400}(T)$ into equation 24, which gave:

$$\mu^2_{400}(T) = 6.9644 \cdot 10^{-19} + 12.049\ 10^{-22} T + 2.0223 \cdot 10^{-24} T^2 - 0.7219 \cdot 10^{-10} T^3. \qquad (28)$$

Here $\mu^2_{hkl}(T)$ is in cm^2 and T is in ^oC. A plot of this function is shown in Figure 10.

The observed intensity and Bragg angle data for the runs made on the zinc c and a axis single crystals are listed in Tables 5 and 6, respectively, in Appendix C. Plots of the natural logarithm of the scaled intensities versus temperature for these runs are shown in Figures 11 to 16. The intensities for the zinc single crystals were scaled by calculating a mean square vibration amplitude for the lowest temperature of measurement from equation 11, using Grüneisen and Goens' (13) values for the Debye temperatures of 200^oK for the direction parallel to the hexagonal c axis and 320^oK for directions perpendicular to the c axis, and then calculating a scaling factor K from equation 22. Also shown on these plots are the curves representing the least squares fit of equation 25 to the data. Most of the intensity values agree with the least squares curve to within $\pm 3\%$ for runs Xb and XIV, to within $\pm 5\%$ for runs XII and XIIIb, to within $\pm 7\%$ for run XIIIa, and to within $\pm 10\%$ for run XVIII.

The change of the (0006) reflection intensity with temperature is

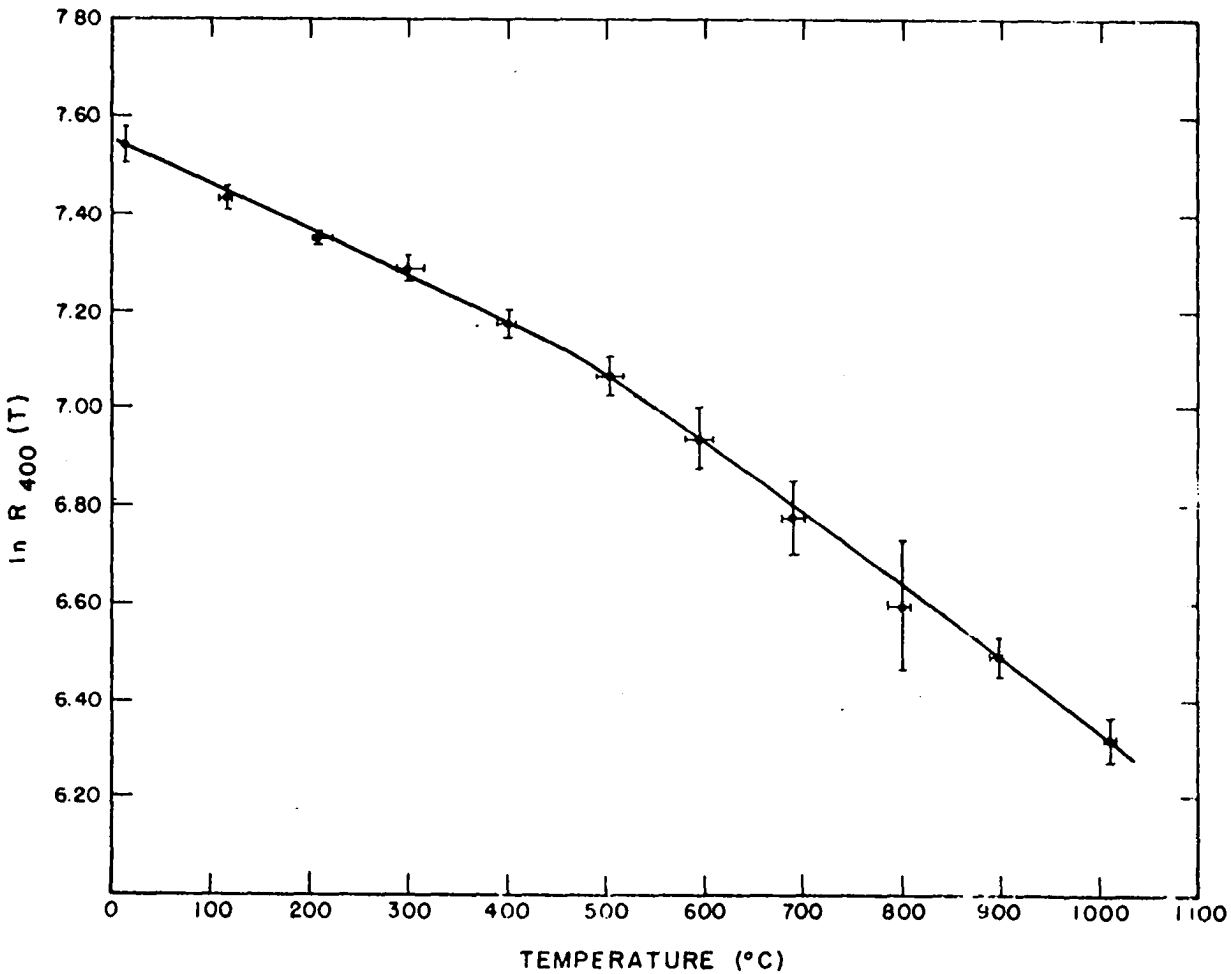

Figure 9. Mean values of ln $R_{400}(T)$ and standard deviations versus temperature for copper. All runs

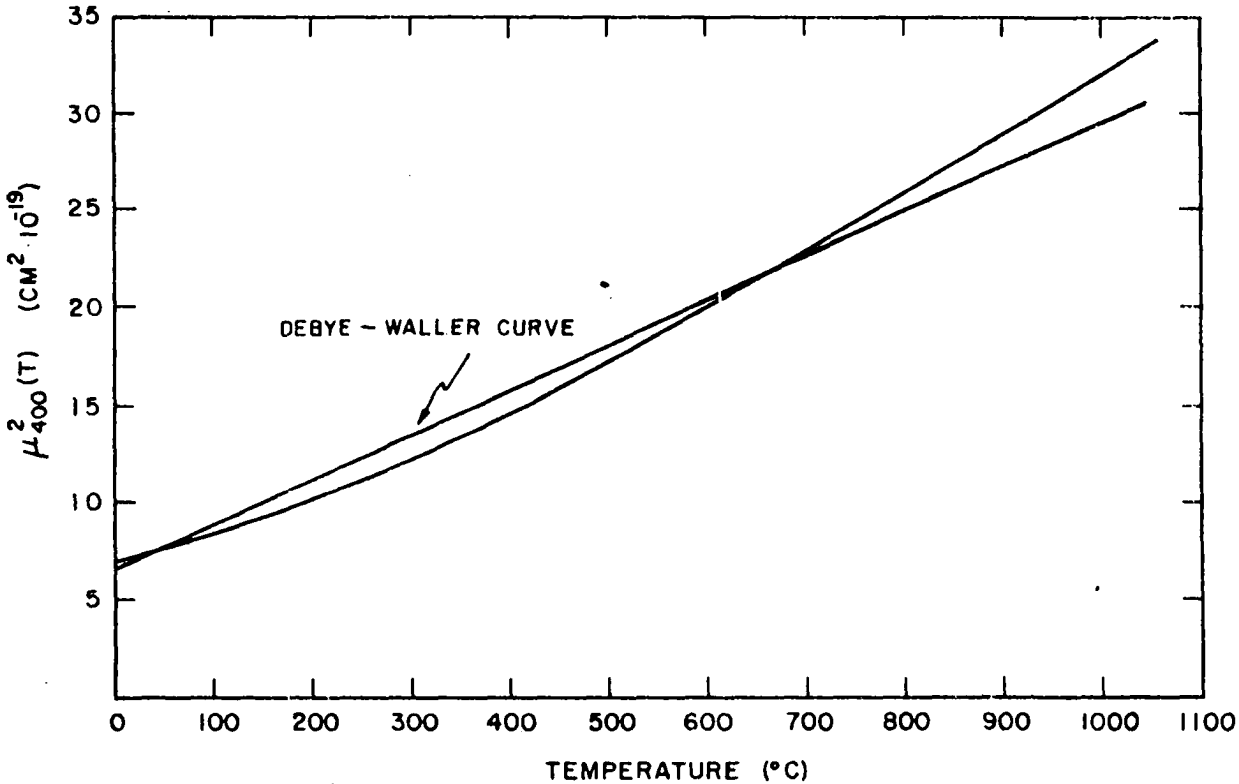

Figure 10. $\mu^2_{400}(T)$ versus temperature for copper

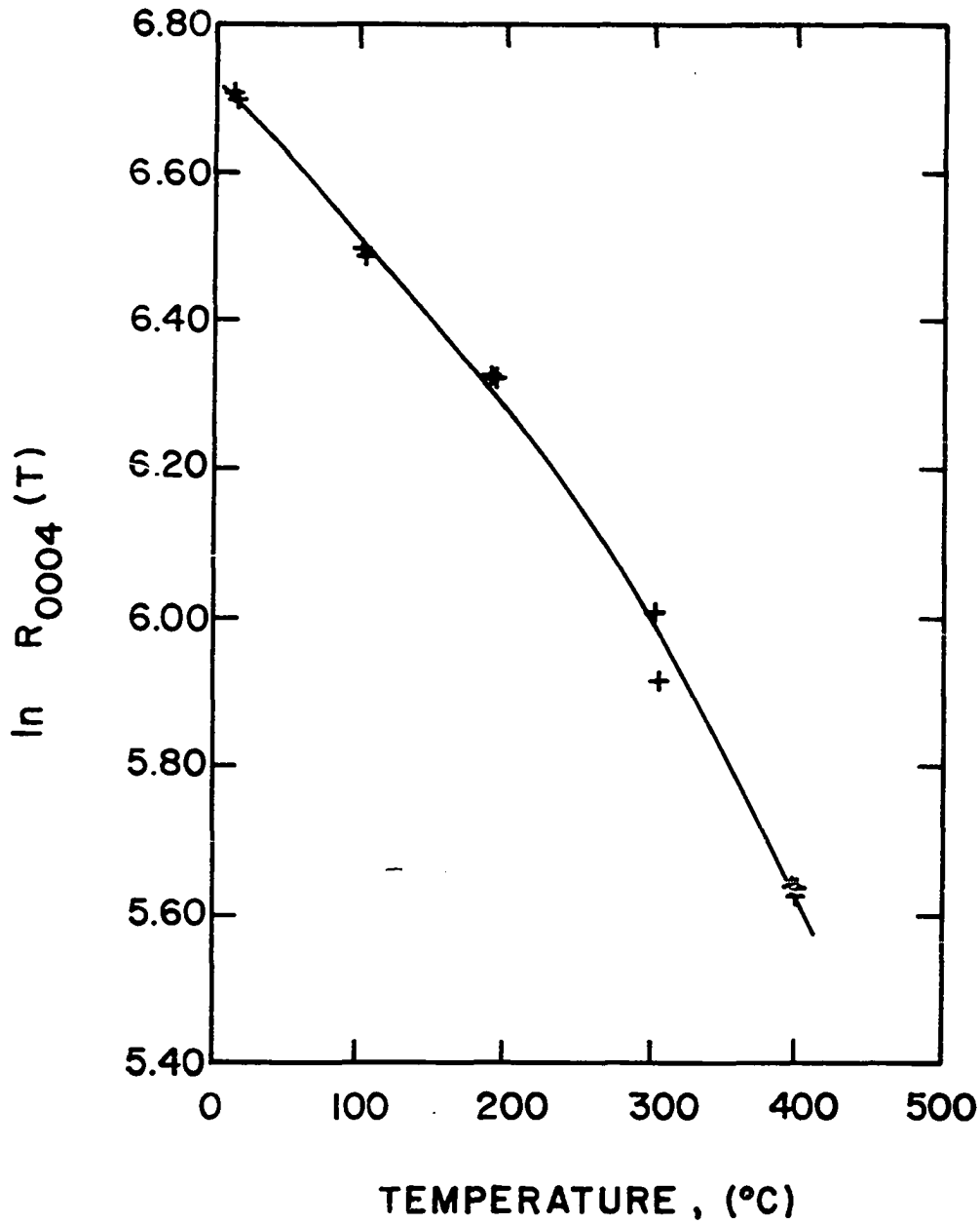

Figure 11. ln $R_{0004}(T)$ versus temperature for zinc. Run Xb

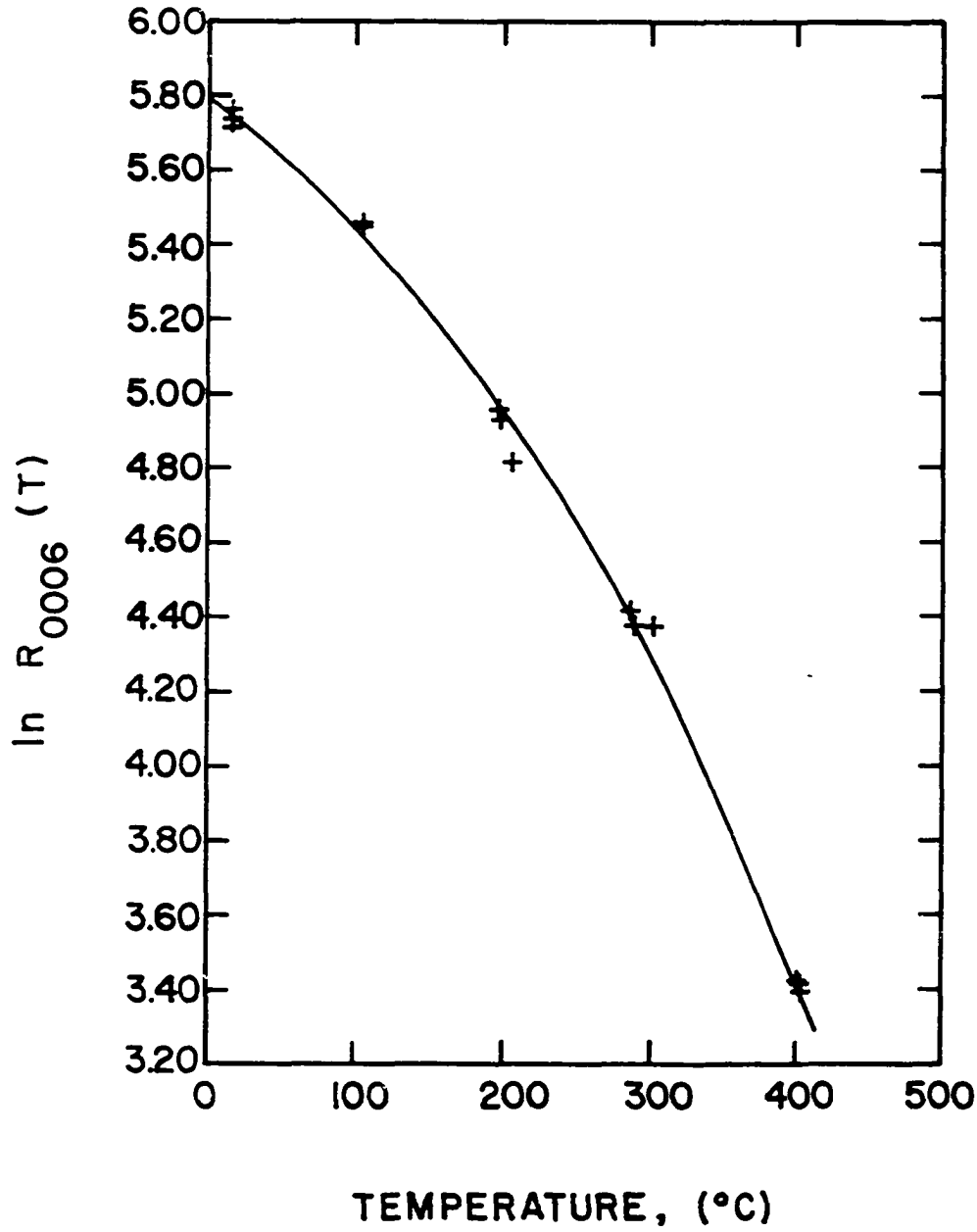

Figure 12. ln $R_{0006}(T)$ versus temperature for zinc. Run XII

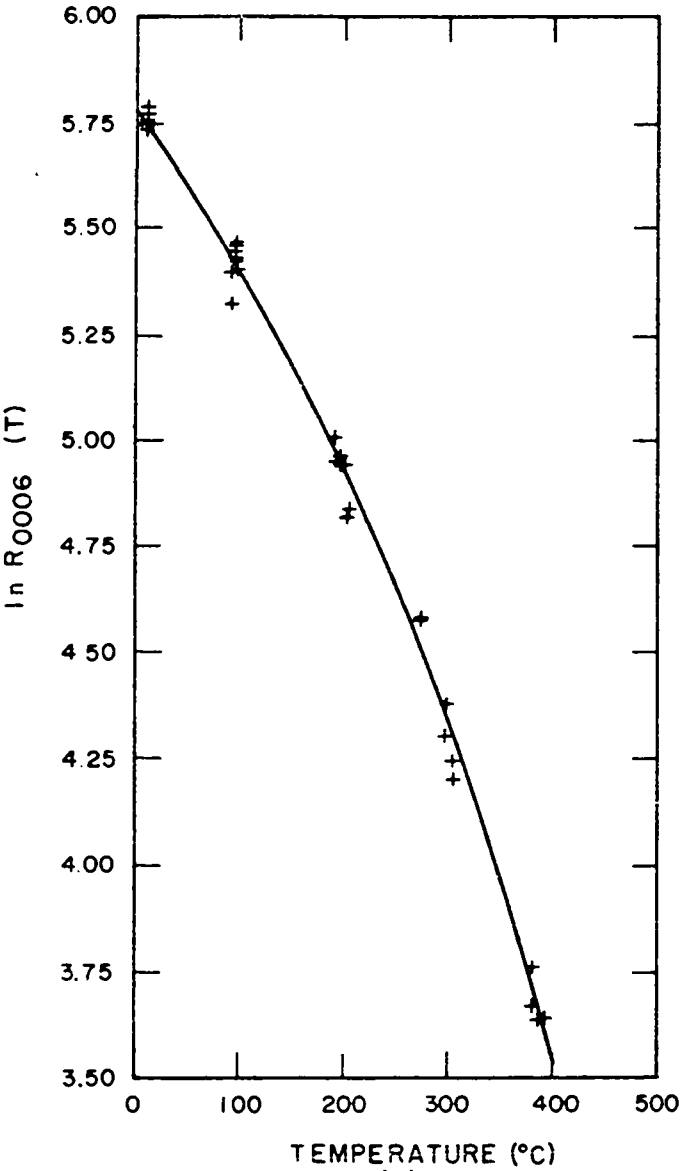

Figure 13. ln $R_{0006}(T)$ versus temperature for zinc. Run XIIIa

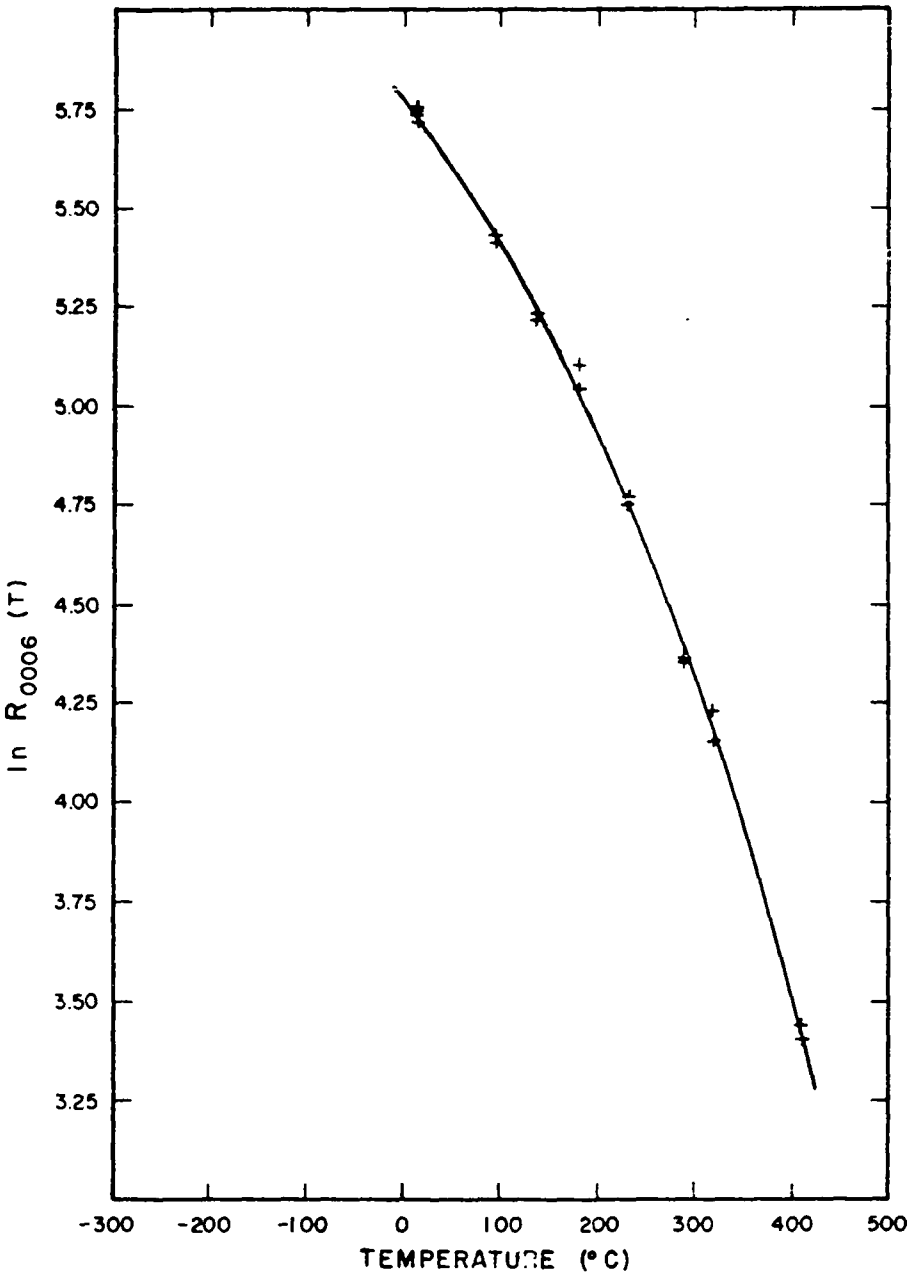

Figure 14. ln $R_{0006}(T)$ versus temperature for zinc. Run XIIIb

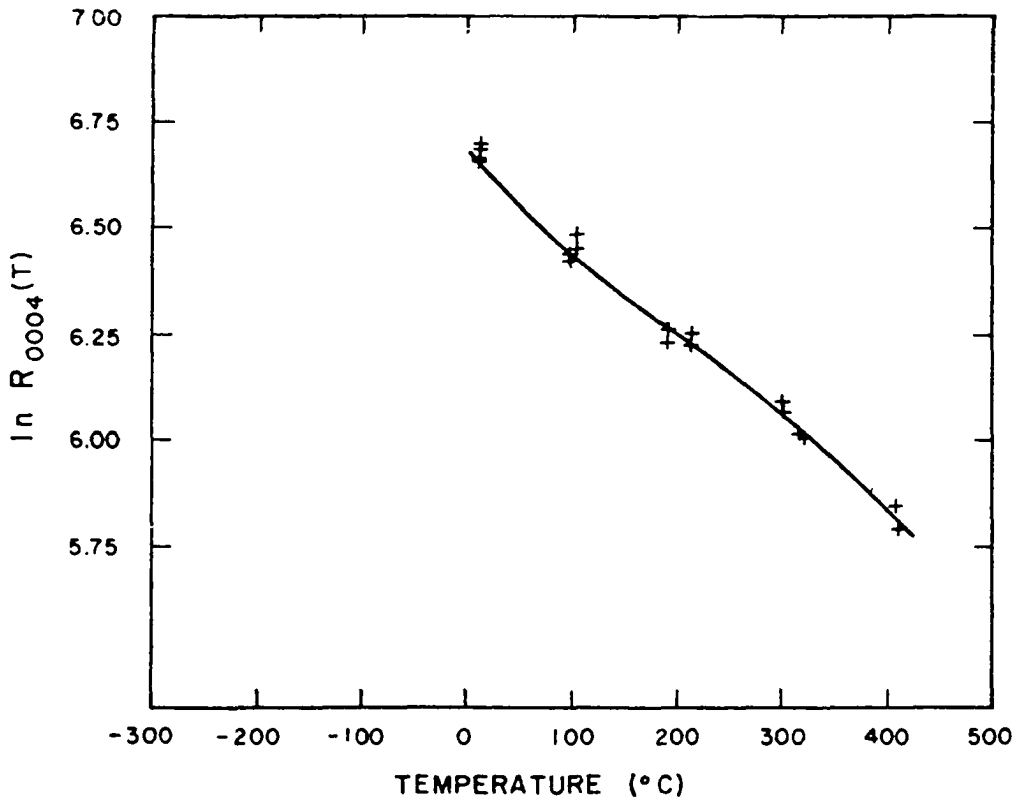

Figure 15. ln $R_{0004}(T)$ versus temperature for zinc. Run XIV

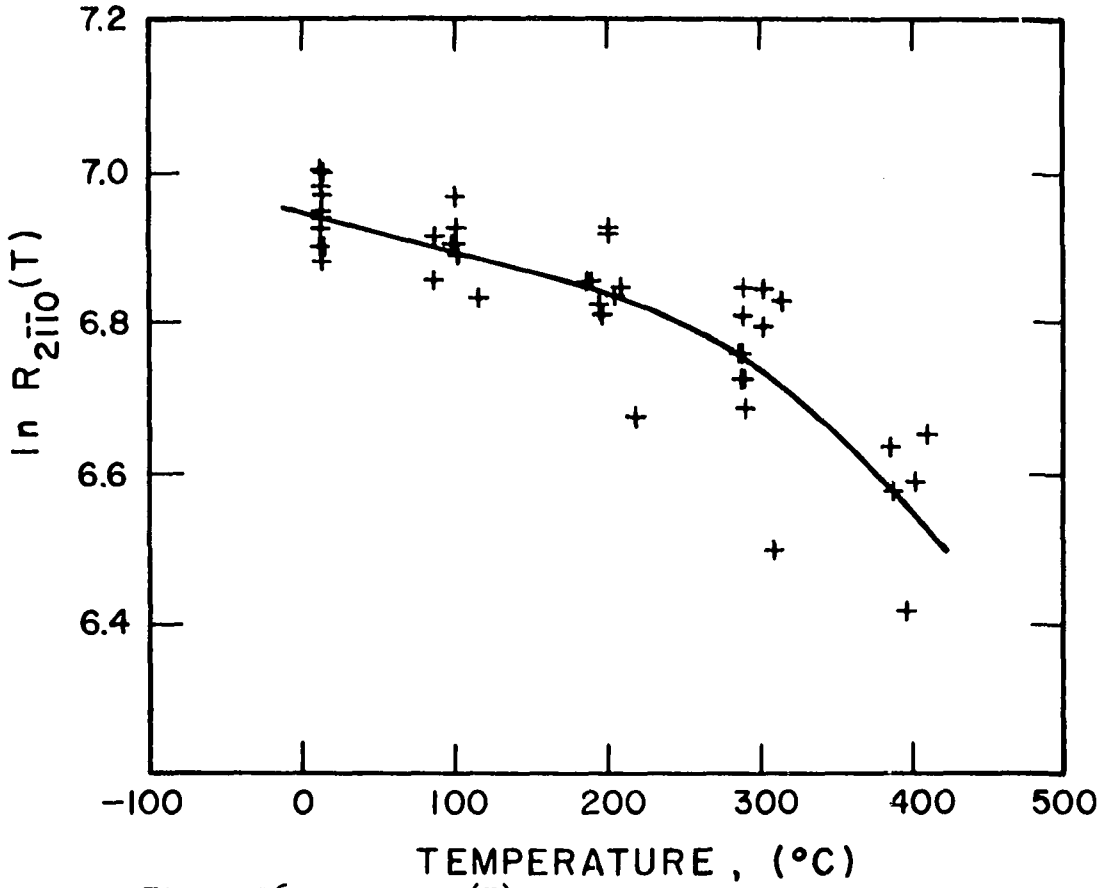

Figure 16. ln $R_{2\bar{1}\bar{1}0}(T)$ versus temperature for zinc. Run XVIII

larger than for lower-angle reflections. Therefore, the data of runs XII, XIIIa, and XIIIb were chosen to be scaled together, and these are plotted in Figure 17, along with the least squares fit of equation 25 to the combined data. Most of the intensity values are within $\pm 6\%$ of the least squares curve in this plot. The resulting equation for the function $\ln R_{0006}(T)$ is:

$$\ln R_{0006}(T) = 5.5584 - 3.7238 \cdot 10^{-3} T - 8.9406 \cdot 10^{-7} T^2 - 1.0249 \cdot 10^{-8} T^3. \quad (29)$$

The equation for the function $\ln R_{2\bar{1}\bar{1}0}(T)$ from run XVIII is:

$$\ln R_{2\bar{1}\bar{1}0}(T) = 6.9496 - 7.1009 \cdot 10^{-4} T + 2.3858 \cdot 10^{-6} T^2 - 7.8106 \cdot 10^{-9} T^3. \quad (30)$$

The equations for the mean square amplitude of vibration in the $\underline{c}$ and $\underline{a}$ axes can be calculated by substituting equations 29 and 30 in turn into equation 24. Thus:

$$\mu^2_{0006}(T) = 15.1085\ 10^{-19} + 6.4091 \cdot 10^{-21} T + 1.5388 \cdot 10^{-24} T^2 + 1.7639 \cdot 10^{-26} T^3 \quad (31)$$

$$\mu^2_{2\bar{1}\bar{1}0}(T) = 5.7295 \cdot 10^{-19} + 3.1579 \cdot 10^{-21} T - 1.0610 \cdot 10^{-23} T^2 + 3.4736 \cdot 10^{-26} T^3, \quad (32)$$

where $\mu^2_{hkl}(T)$ is in cm^2 and T is in $^{\circ}C$. These functions are shown in Figure 18.

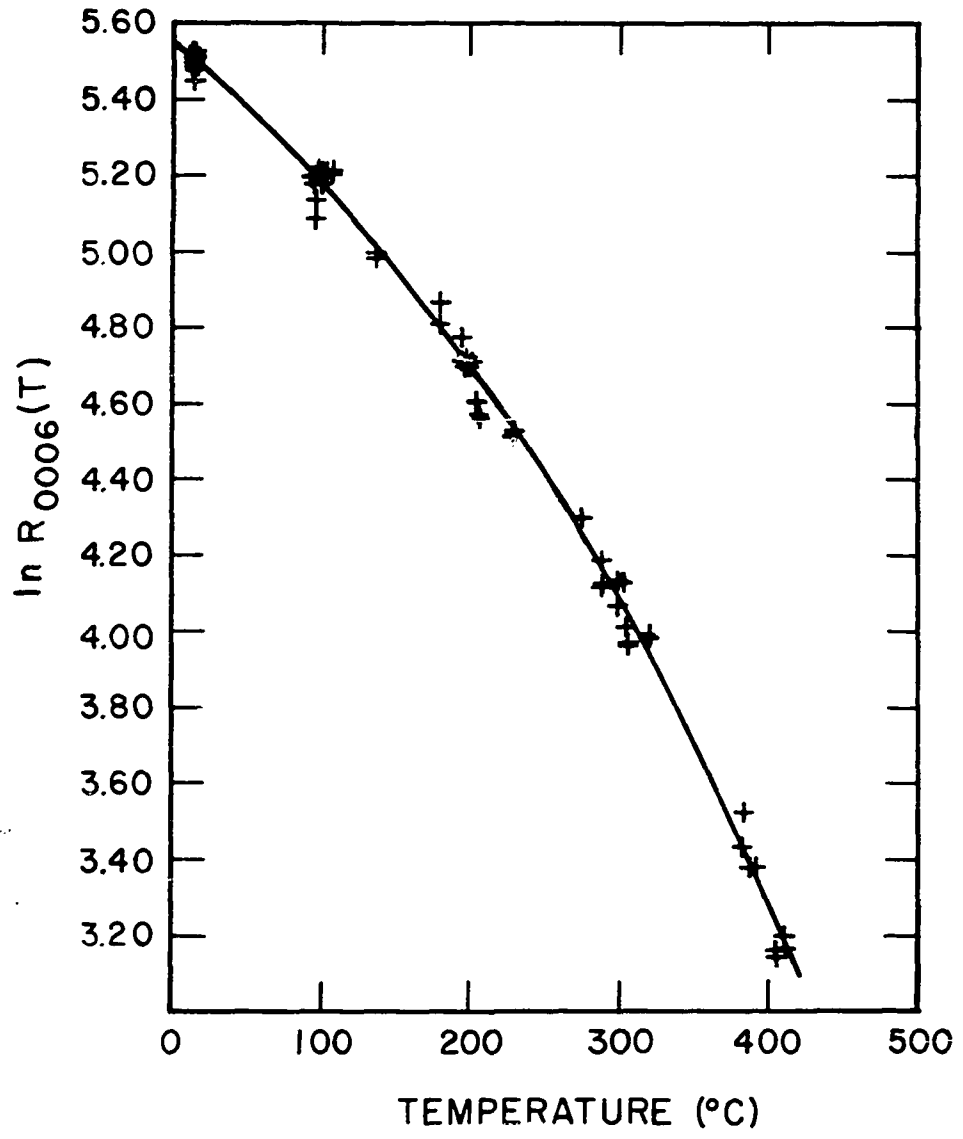

Figure 17. ln $R_{0006}(T)$ versus temperature for zinc. All runs

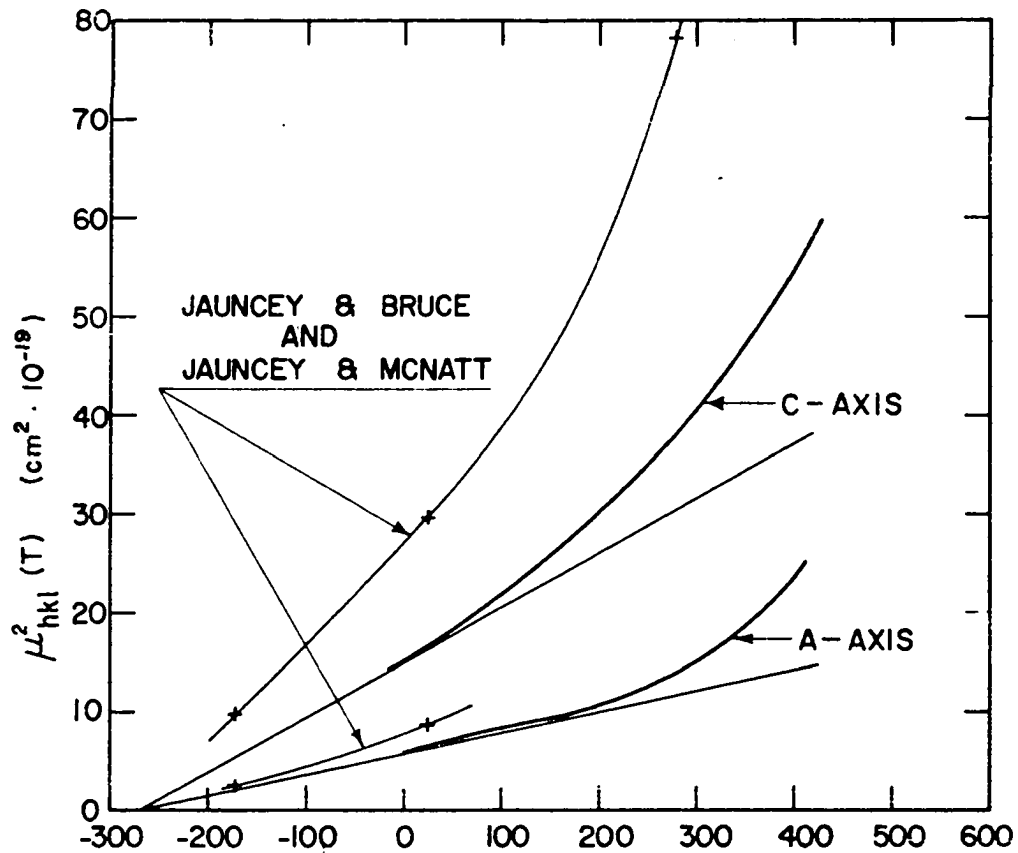

Figure 18. $\mu^2_{hkl}(T)$ versus temperature for zinc in the directions parallel to the c and a axes

B. Thermal Expansion

In Figure 19 are shown the combined results of runs XVa, XVb, and XVc for the change in the interplanar spacing with the temperature for the (400) planes in copper. Also shown is the least squares curve representing the fit of the function:

$$d_{hkl}(T) = \sum_{n=0}^{2} a_n T^n \qquad (33)$$

to the data. The equation for this curve is:

$$d_{400} = (0.903396 \pm 0.000053) + (1.231 \pm 0.026)\cdot 10^{-5} T + (3.56 \pm 0.26)\cdot 10^{-9} T^2, \qquad (34)$$

where d_{400} is in Angstrom units and T in $^{\circ}C$. All the data are within $\pm 0.07\%$ of the least squares curve.

Figures 20 to 24 show the thermal expansion results for the zinc runs. For these runs the data are all within $\pm 0.02\%$ of the least squares curve, except for run XIIIa. For run XIIIa, this value is $\pm 0.03\%$. The equations of these least squares curves are:

$$\text{Run XII} - d_{0006} = (0.823478 \pm 0.000053) + (5.055 \pm 0.065)\cdot 10^{-5} T - (7.60 \pm 1.5)\cdot 10^{-9} T^2 \qquad (35)$$

$$\text{Run IIIa} - d_{0006} = (0.823238 \pm 0.000058) + (4.842 \pm 0.079)\cdot 10^{-5} T - (3.41 \pm 1.9)\cdot 10^{-9} T^2 \qquad (36)$$

$$\text{Run IIIb} - d_{0006} = (0.823037 \pm 0.000030) + (5.504 \pm 0.035)\cdot 10^{-5} T - (7.64 \pm 0.85)\cdot 10^{-9} T^2 \qquad (37)$$

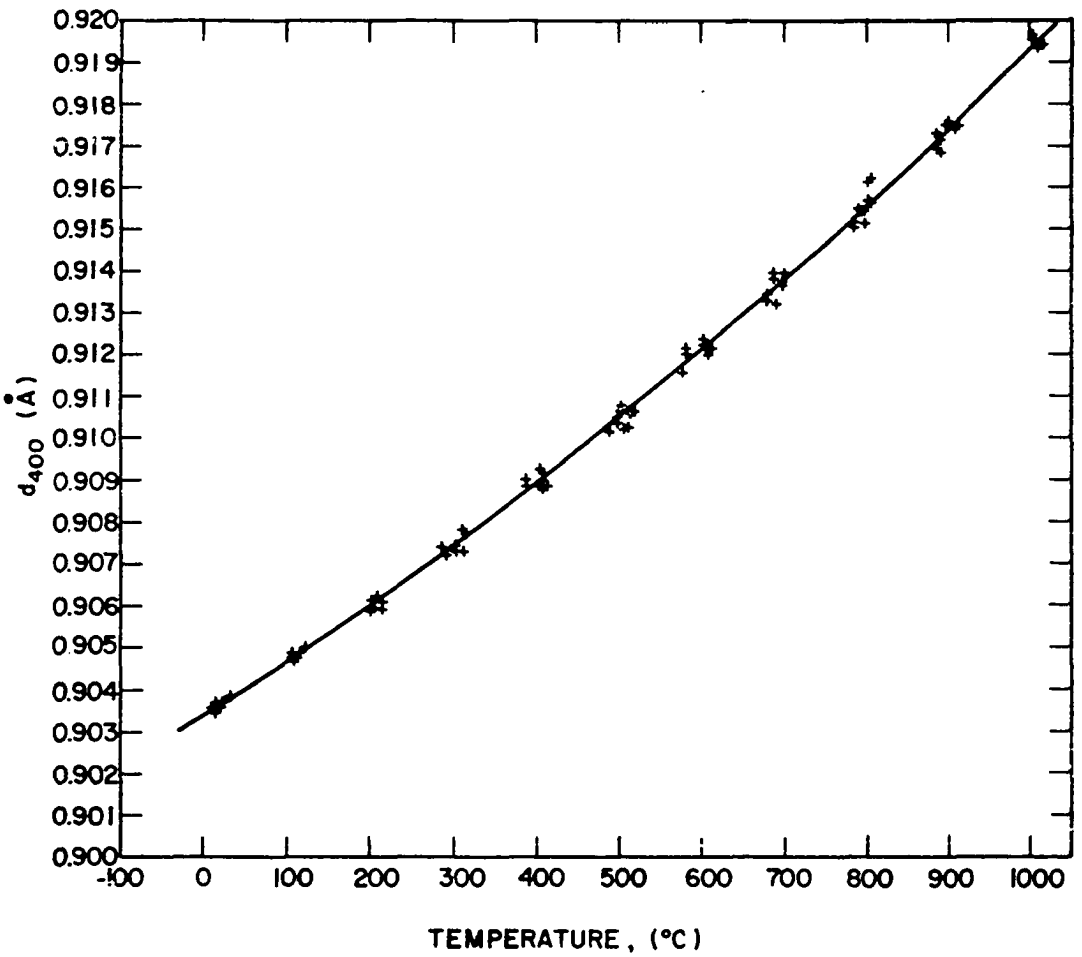

Figure 19. (400) interplanar spacing versus temperature for copper

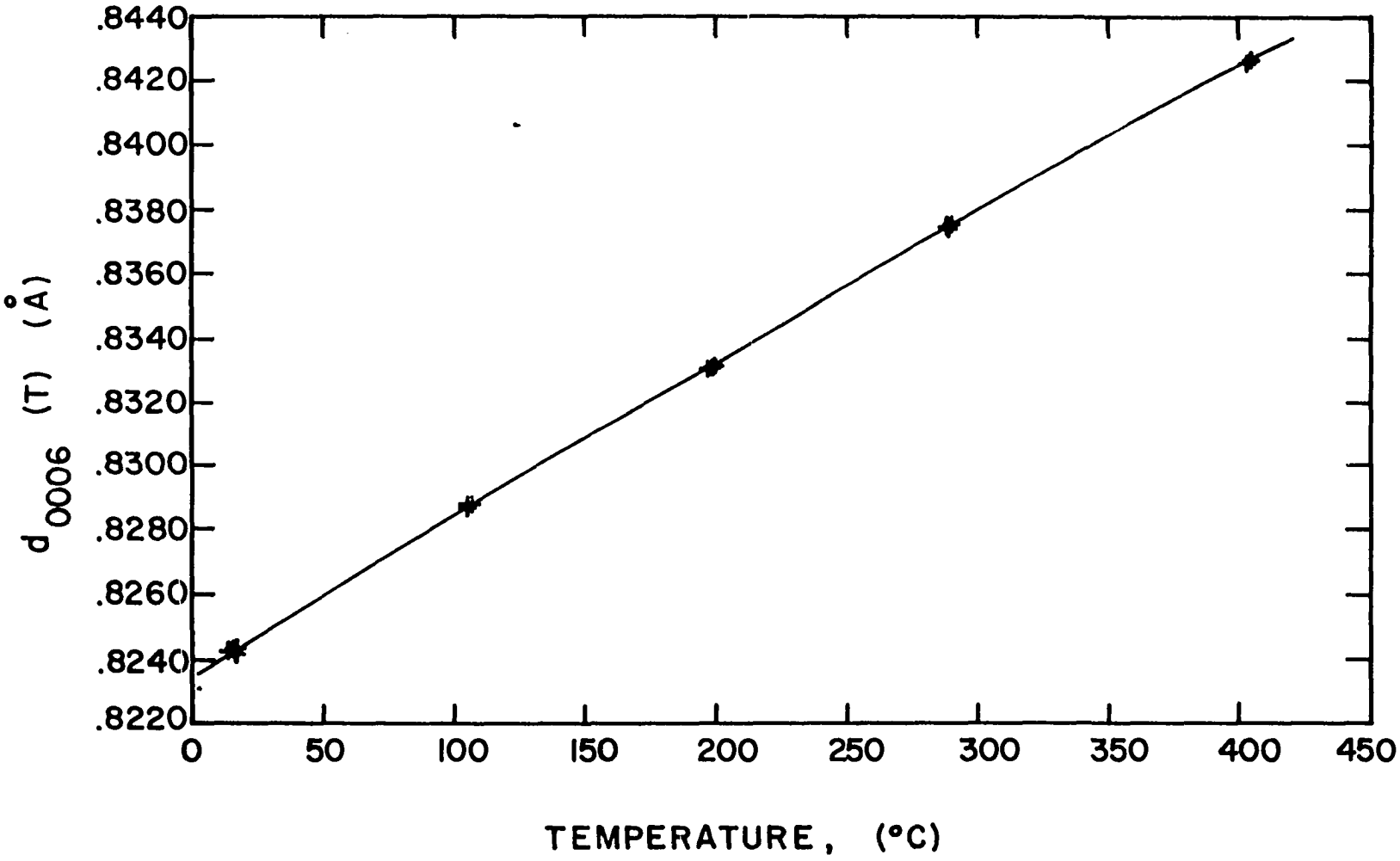

Figure 20. (0006) interplanar spacing versus temperature for zinc. Run XII

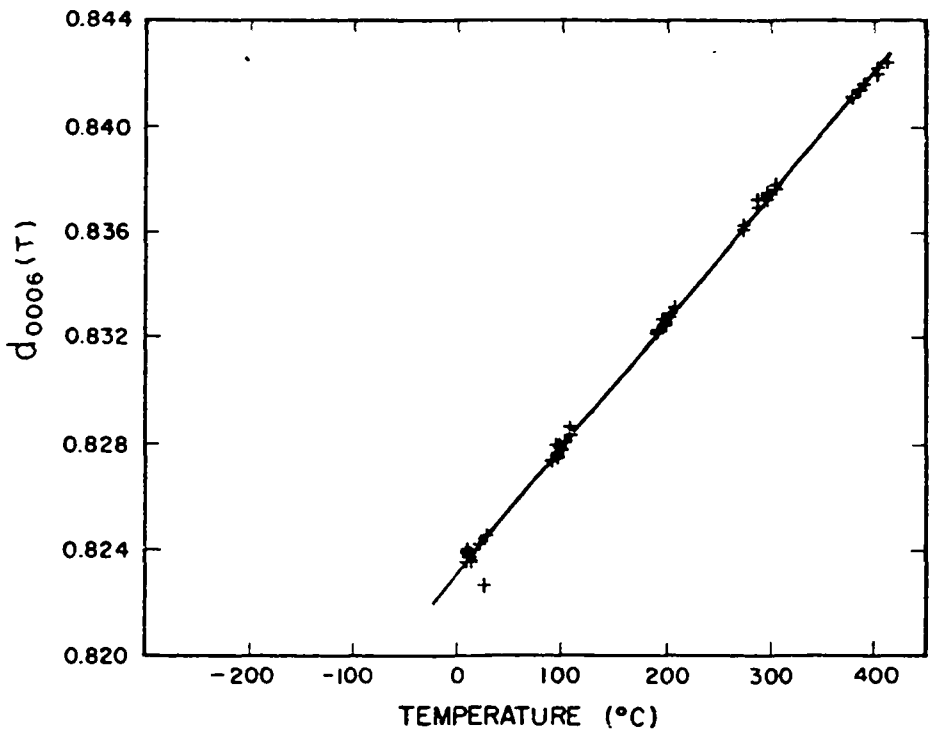

Figure 21. (0006) interplanar spacing vertus temperature for zinc. Run XIIIa

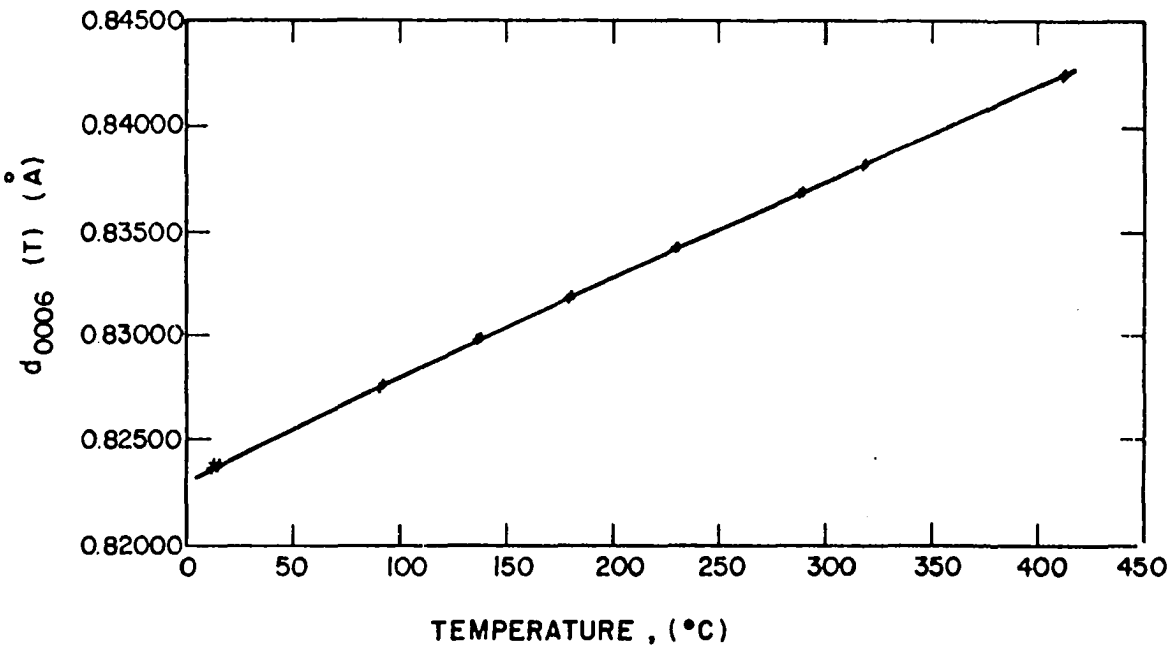

Figure 22. (0006) interplanar spacing versus temperature for zinc. Run XIIIb

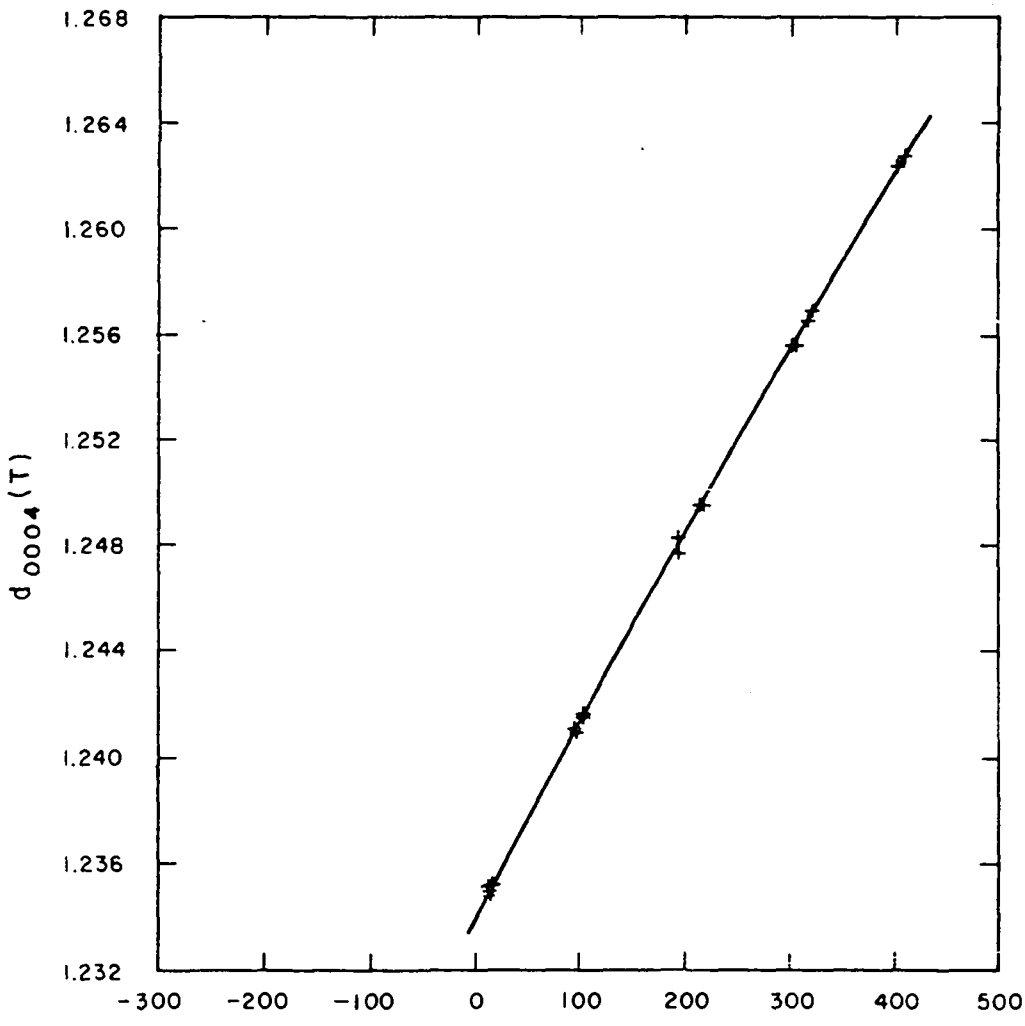

Figure 23. (0004) interplanar spacing versus temperature for zinc. Run XIV

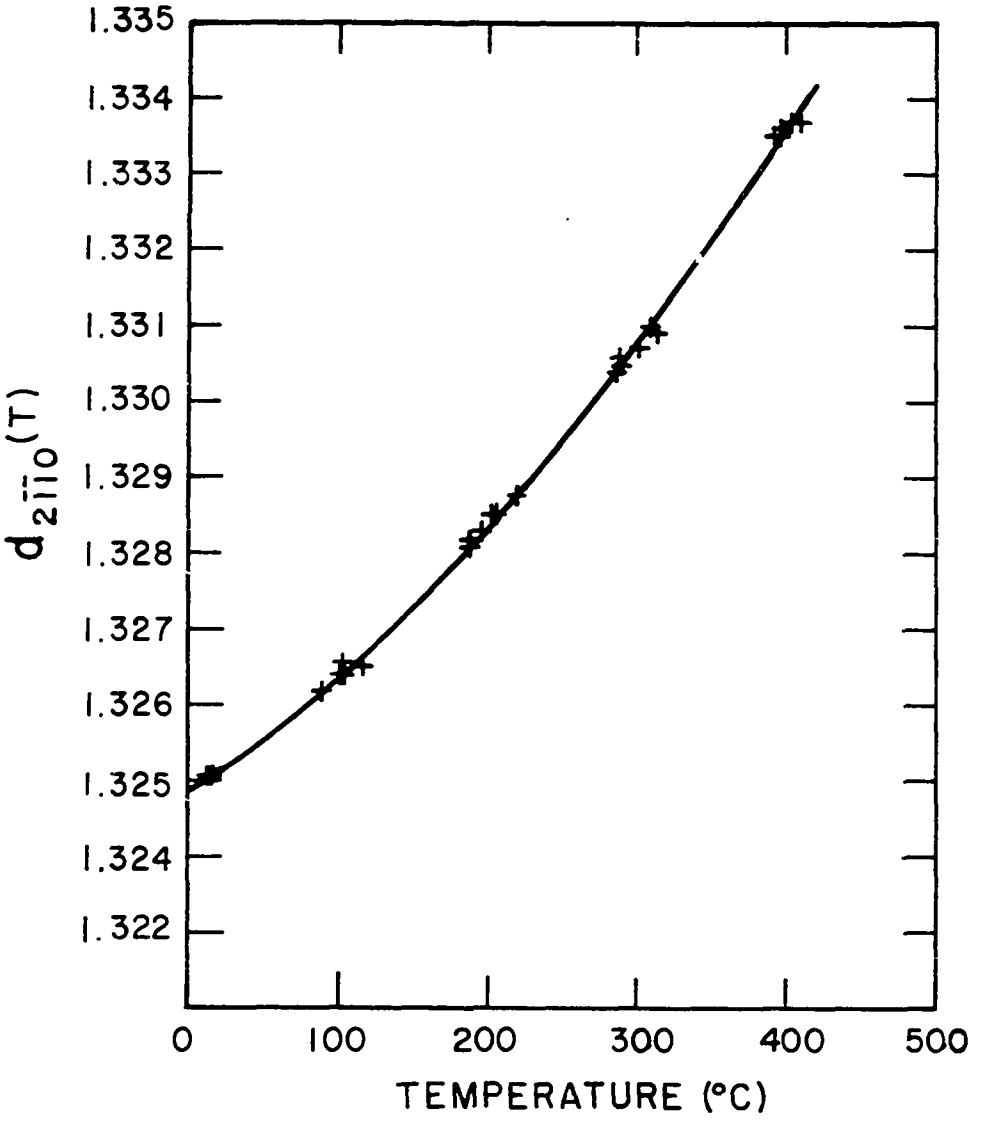

Figure 24. $(2\bar{1}\bar{1}0)$ interplanar spacing versus temperature for zinc. Run XVIII

$$\text{Run XIV} - d_{0004} = (1.233918 \pm 0.000053) + (7.494 \pm 0.065)\cdot 10^{-5} T - (1.20 \pm 0.15)\cdot 10^{-9} T^2 \qquad (38)$$

$$\text{Run XVIII} - d_{2\bar{1}\bar{1}0} = (1.324878 \pm 0.000089) + (1.20 \pm 0.11)\cdot 10^{-5} + (2.47 \pm 0.28)\cdot 10^{-8} T^2 \qquad (39)$$

C. Discussion of Results

Considerable difficulty was encountered in obtaining intensity measurements which were reproducible between runs. A comparison of the curves in Figures 4 to 7 for the four runs made on the copper single crystal shows that the temperature dependence is different for each run. The scatter in the individual runs is of the order of 2 - 4%. The standard deviations shown in Figure 9 for the combined copper data range from ± 0.013 to ± 0.130. This corresponds to fractional deviations from the mean intensity values of $\pm 2.4\%$ to $\pm 11\%$.

A probable explanation for this difficulty is that the mosaic structure of the crystal changes with the thermal history of the sample. Most real crystals are considered to be neither perfect nor ideally mosaic where the crystal is composed of small perfect blocks of material slightly misoriented with respect to one another. They are considered to consist of crystal planes which are warped due to a network of dislocations throughout the crystal. James (1), Chapter II, describes in detail the theory of the diffraction of x-rays by both a perfect crystal and an ideal mosaic crystal. His calculations in Chapter VI show that the integrated intensity of reflection from an ideal mosaic crystal of

aluminum would have from five to forty times the intensity from a perfect crystal of aluminum, depending upon which reflection is examined. The experimental measurements of James, Brindley, and Wood (8) on single crystals of aluminum give values intermediate between the values calculated for the two ideal states of the crystal. If the mosaic structure of a crystal changed from nearly perfect to nearly ideally mosaic, or vice versa, a very large difference in the reflection intensity between the two states would be observed.

Consequently, at any particular temperature relatively small changes in the degree of perfection of the single crystals used in this investigation could produce noticeable variations in the integrated intensities. Thermal stresses are created in the single crystal during heating and cooling and motion of dislocations in the crystal will occur to relieve these stresses. When the single crystal sample is maintained at some temperature, a certain mosaic structure is obtained which is dependent on the thermal history of the crystal. Changes in the substructure of copper were evident upon microscopic examination of the etched crystal surface before and after the crystal had been repeatedly heated and cooled in the course of intensity measurements. These observations strongly suggest that the mosaic structure also varies with thermal history.

The copper single crystal used in this work was cycled between 13°C and 500-1000°C seventeen times. Photomicrographs of the (100) face were taken of the crystal as initially produced and of the sample used after it had been cycled seventeen times.

The surface in each case was etched in concentrated nitric acid and photographed at a magnification of 256x. The etched surface of the crystal that had not been thermally cycled showed only a rough surface due to the deep etching. Figures 25 and 26 are photographs of the cycled sample taken near the edge and near the center of the crystal face, respectively. Figure 25 shows a series of square mounds with the same orientation, each mound exhibiting a structure characteristic of layers around a screw dislocation. Figure 26 shows a similar structure on a much smaller scale, with rows of pits or mounds.

This crystal showed a number of small grains that had formed at the edges of the sample. The sample was examined after the completion of run XVc, before it had been thermally cycled several more times, and no grain structure was present. Also, one of the cleaved c axis zinc crystals examined for use in this investigation showed a grain misoriented about 20° with respect to the surrounding sample after it had been heated to 400°C twice.

The above observations are strong indications that the substructure of the crystals is altered by the thermal stresses induced in the sample during thermal cycling. Thus, significant differences in the values of the intensities measured during the runs can be expected.

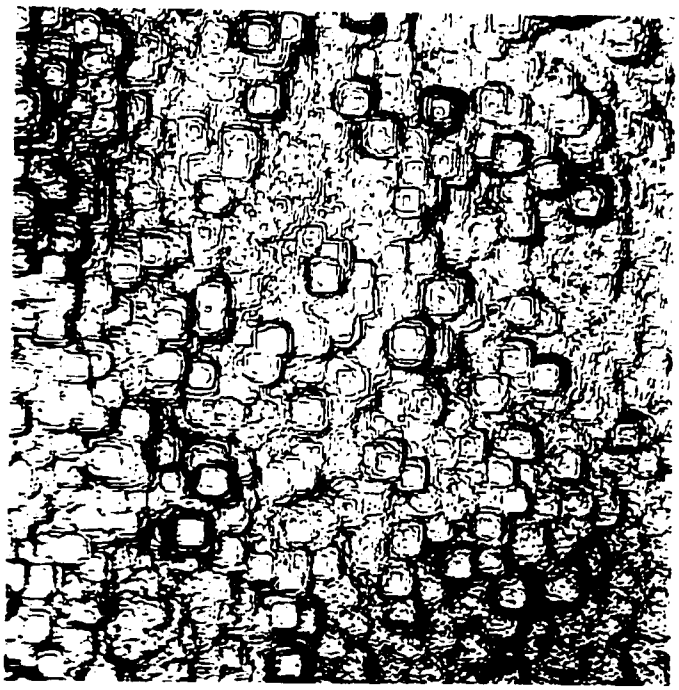

Figure 25. Photomicrograph of surface of copper single crystal near edge of sample. 256x. Etched in conc. HNO_3

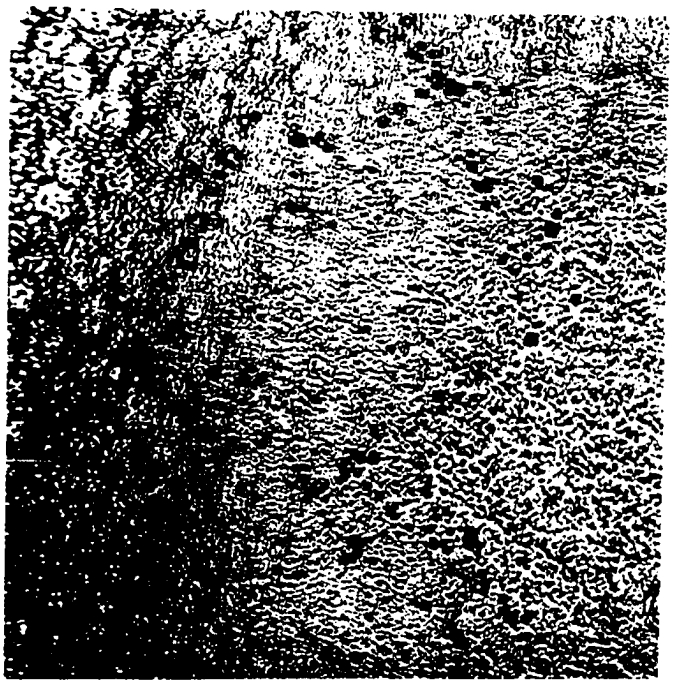

Figure 26. Photomicrograph of surface of copper single crystal near center of sample. 256x. Etched in conc. HNO_3

IV. THEORETICAL CONSIDERATIONS

The Debye-Waller theory predicts that, at high temperatures and at constant volume, the function $\ln R_{hkl}(T)$ is linearly dependent upon the temperature, and that a Debye temperature Θ_M can be calculated from the slope of the resulting straight line. Paskin has modified the Debye-Waller equation to include the volume dependence of the characteristic temperature Θ_M, so that:

$$\ln R_{hkl}(T) = \Gamma^2 \frac{3h^2}{mk\Theta_o^2} \left(\frac{V(T)}{V(T_o)}\right)^{2\gamma} T \qquad (40)$$

He has shown that, in the cases of KCl and NaCl, plots of $\ln R_{hkl}$ versus the reduced temperature defined by equation 19 gives straight lines. The intensity data obtained in this investigation for copper and zinc can be examined in this way to see how well the modified Debye-Waller expression fits the experimental results. It should be noted, however, that since the Debye model assumes an isotropic continuous solid, and zinc is anisotropic, the theory is not really expected to adequately explain the decrease with temperature of the reflection intensity for this metal.

The mean values shown in Figure 9 for the groups of intensity data for the copper single crystal were plotted against the reduced temperature. The change with temperature of the (400) interplanar spacing was used to calculate the reduced temperature, with the interplanar spacing of 14°C taken as the base value. The value of 1.9 for the Grüneisen constant was taken from Darken and Gurry (14), page 159. The

results are shown in Figure 27. The points do not lie on a straight line. However, a straight line corresponding to a least squares fit to these points passes within the range of standard deviation of nearly all the mean values. The Debye temperature Θ_o calculated from the slope of this line, using equation 40, is $329^\circ \pm 4^\circ K$, which agrees approximately with the value of $315^\circ K$ obtained from specific heat measurements. The least squares curve of the function $\ln R_{400}(T)$ is also shown in Figure 27 plotted against the reduced temperature. This curve is linear from 400° to $1000^\circ C$, but below $400^\circ C$ the slope of the curve gradually increases as the temperature approaches $0^\circ C$. The value of the Debye temperature Θ_o at $13^\circ C$ based upon the slope of the linear portion of this curve from 400° to $1000^\circ C$ is $321^\circ K$. It is felt that the modified Debye-Waller expression fits the data fairly well, and thus the change of the characteristic temperature for copper can be represented by the relation:

$$\frac{\Theta(T)}{\Theta_o} = \left(\frac{V(T_o)}{V(T)}\right)^{\gamma} . \qquad (41)$$

The Debye temperature as a function of temperature can be evaluated from the intensity data by solving equations 15 and 12 for Θ_M. Figure 28 shows the results of these calculations for the temperature range 13° to $1000^\circ C$. The Debye temperature decreases from a value of over $400^\circ K$ at $13^\circ C$ to $278^\circ K$ at $1000^\circ C$. Above $400^\circ C$ the Debye temperature decreases very slowly. A curve is shown which extrapolates the values above $400^\circ C$ to the previously calculated value of $\Theta_o = 321^\circ K$ at $13^\circ C$.

In the case of zinc, the plots of the natural logarithm of the

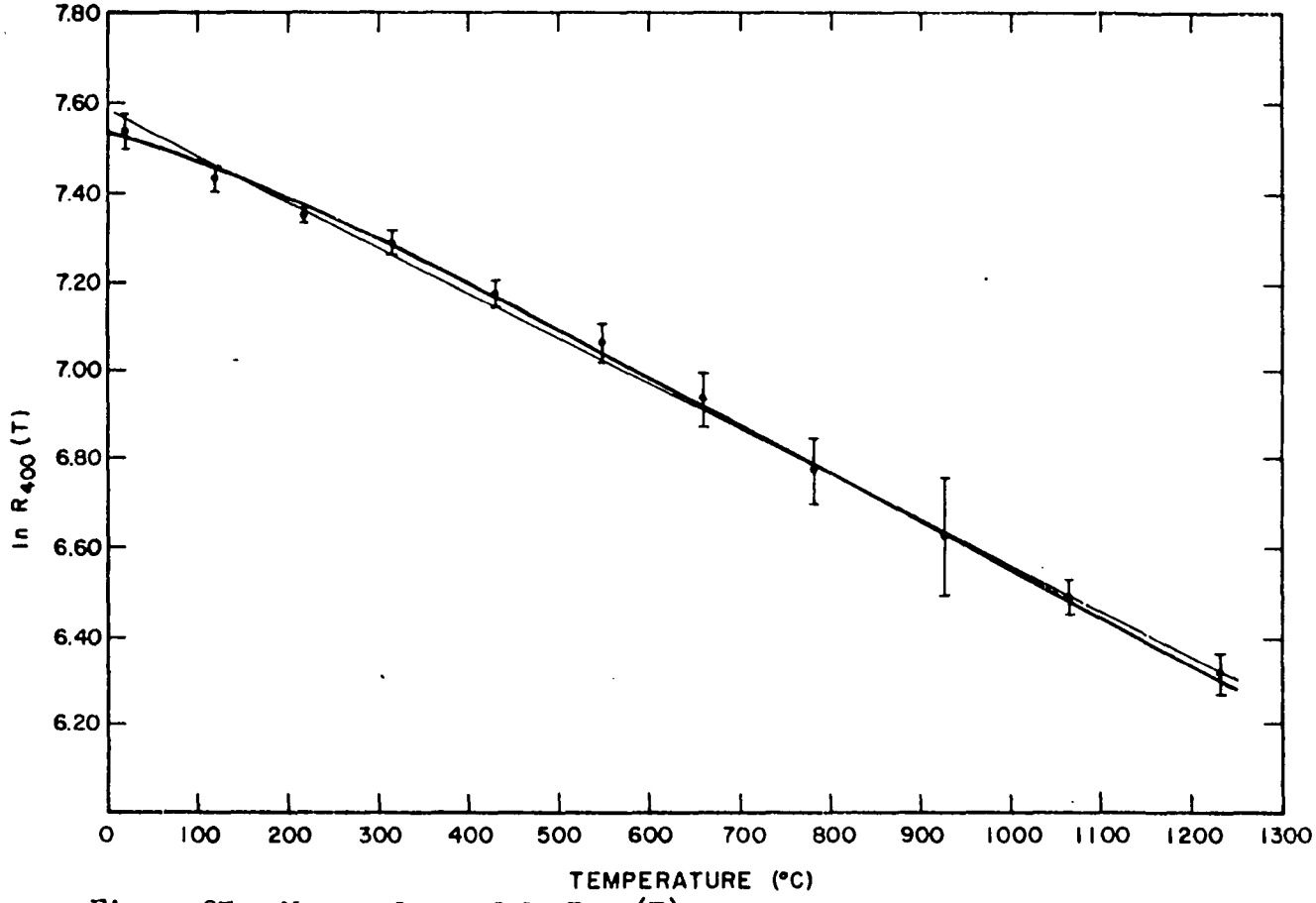

Figure 27. Mean values of ln $R_{400}(T)$ versus reduced temperature for copper

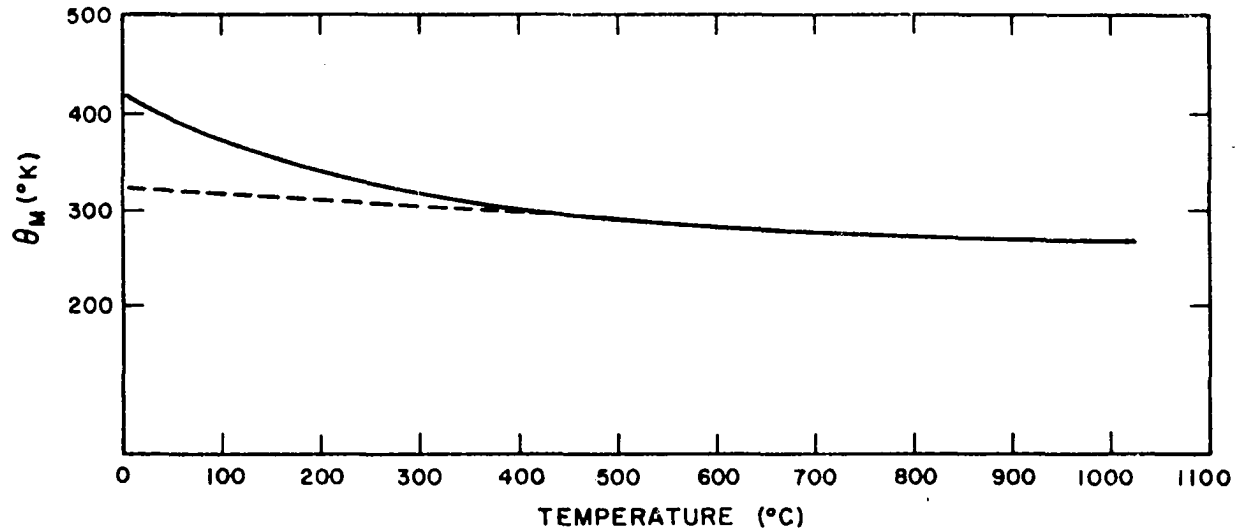

Figure 28. Debye temperature Θ_M versus temperature for copper

(0006) and the $(2\bar{1}\bar{1}0)$ reflection intensities versus the reduced temperature are shown in Figures 29 and 30. The resulting curves are not linear, and it is evident that the modified Debye-Waller expression is inadequate for zinc. The slopes of these curves at 13°C, using equation 40, give values of 191°K and 306°K for the Debye temperatures for the lattice vibrations parallel to the c and a axes, respectively. Grüneisen and Goens' values calculated from elastic constants measurements are 200°K and 320°K.

The mean square vibration amplitudes parallel to the c and a axes can be averaged to obtain an average mean square amplitude for the metal. Thus:

$$\overline{\mu^2} = 8.8558 \cdot 10^{-19} + 4.2416 \cdot 10^{-21} T - 6.5604 \cdot 10^{-24} T^2 + 2.9037 \cdot 10^{-26} T^3 \qquad (42)$$

A plot of this function is shown in Figure 31. Also shown in Figure 31 is a plot of the function in equation 42 versus the reduced temperature. Since this curve is not linear, it is concluded that the modified Debye-Waller expression does not adequately describe the temperature dependence of the average mean square vibration amplitude in zinc.

Plots of the Debye temperature Θ_M as a function of temperature, calculated from equations 15 and 12, for the lattice vibrations parallel to the c and a axes are shown in Figure 32. The Debye temperature for the vibrations parallel to the c axis decreases slowly with increasing temperature, and the Debye temperature for the vibrations parallel to the a axis decreases rapidly with increasing temperature. The validity

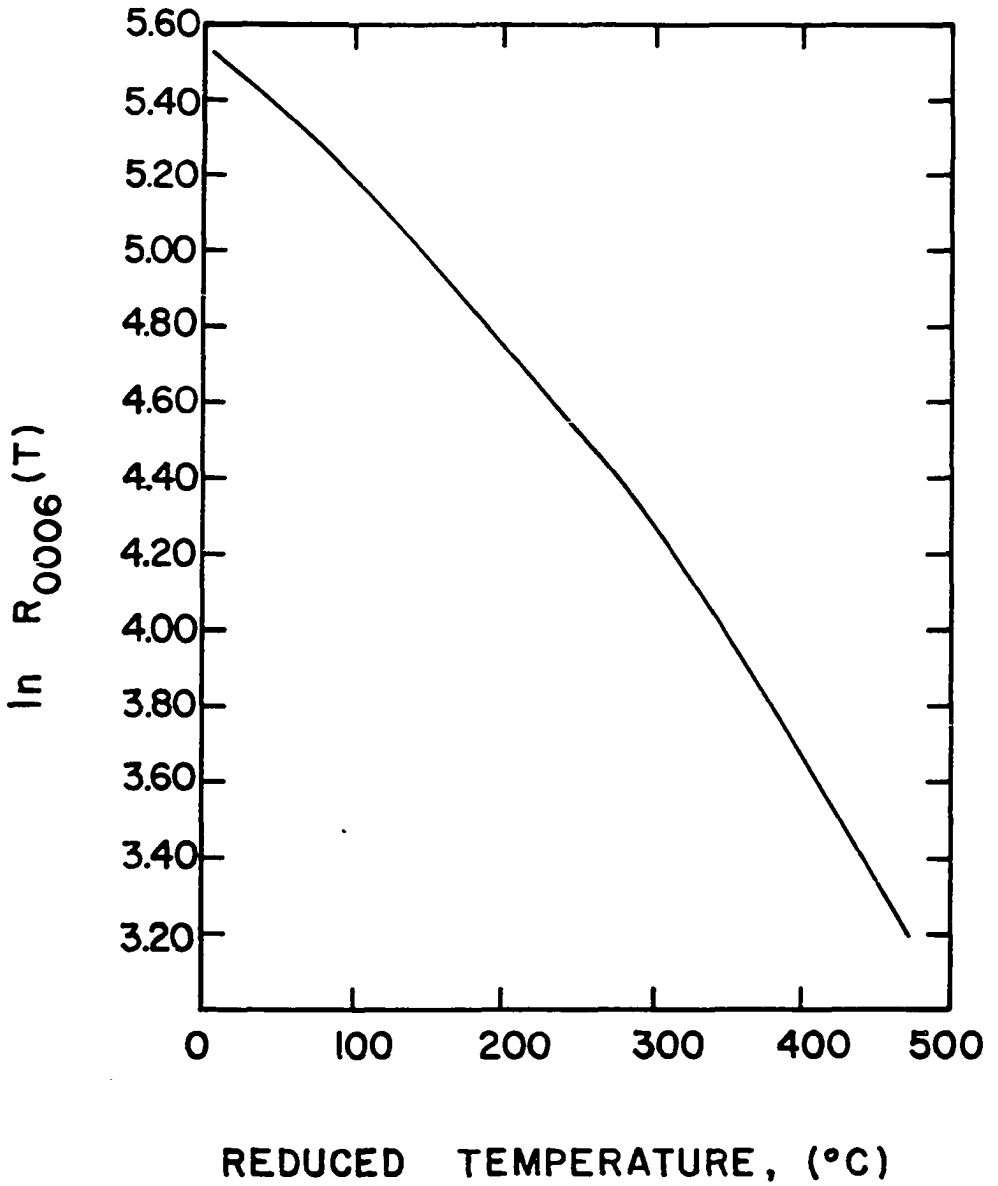

Figure 29. ln $R_{0006}(T)$ versus reduced temperature for zinc

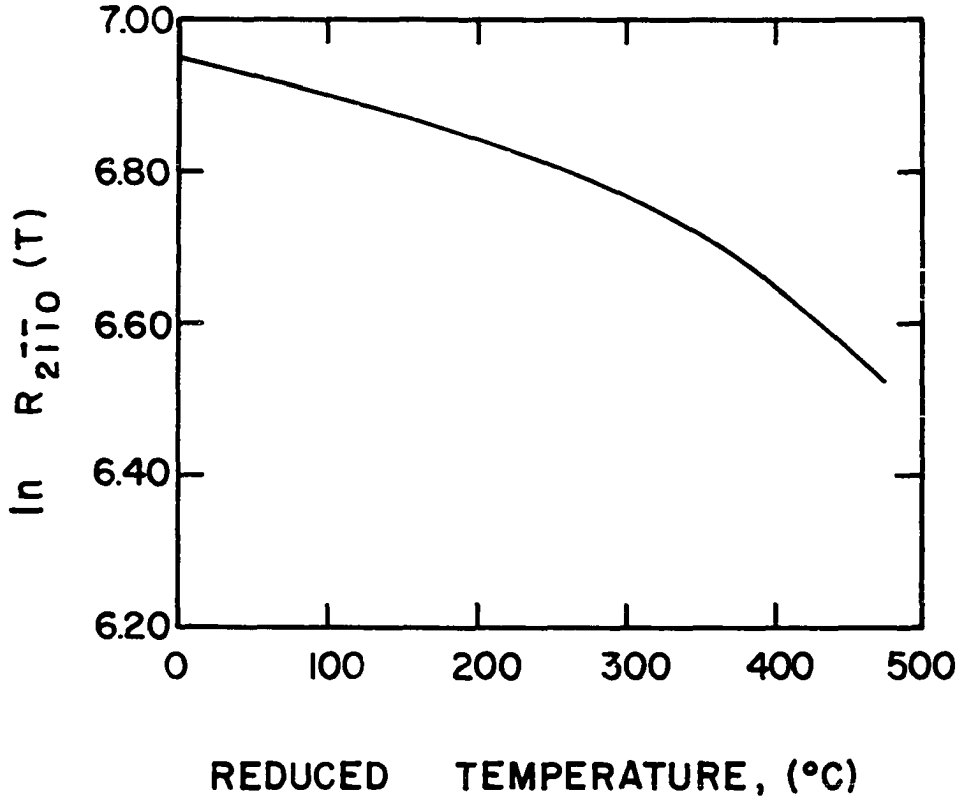

Figure 30. ln $R_{2\bar{1}\bar{1}0}(T)$ versus reduced temperature for zinc

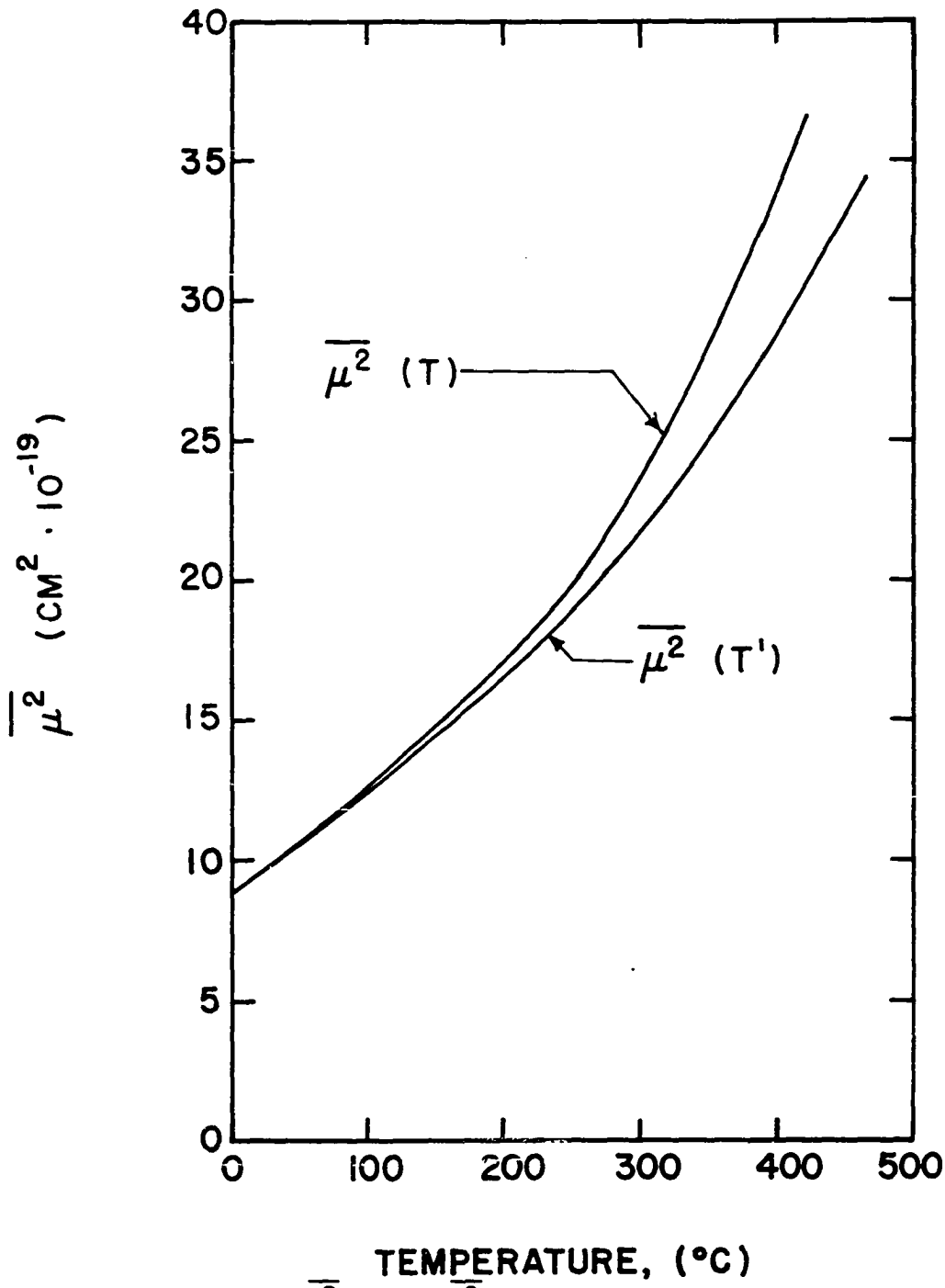

Figure 31. $\overline{\mu^2}(T)$ and $\overline{\mu^2}(T')$ versus temperature for zinc

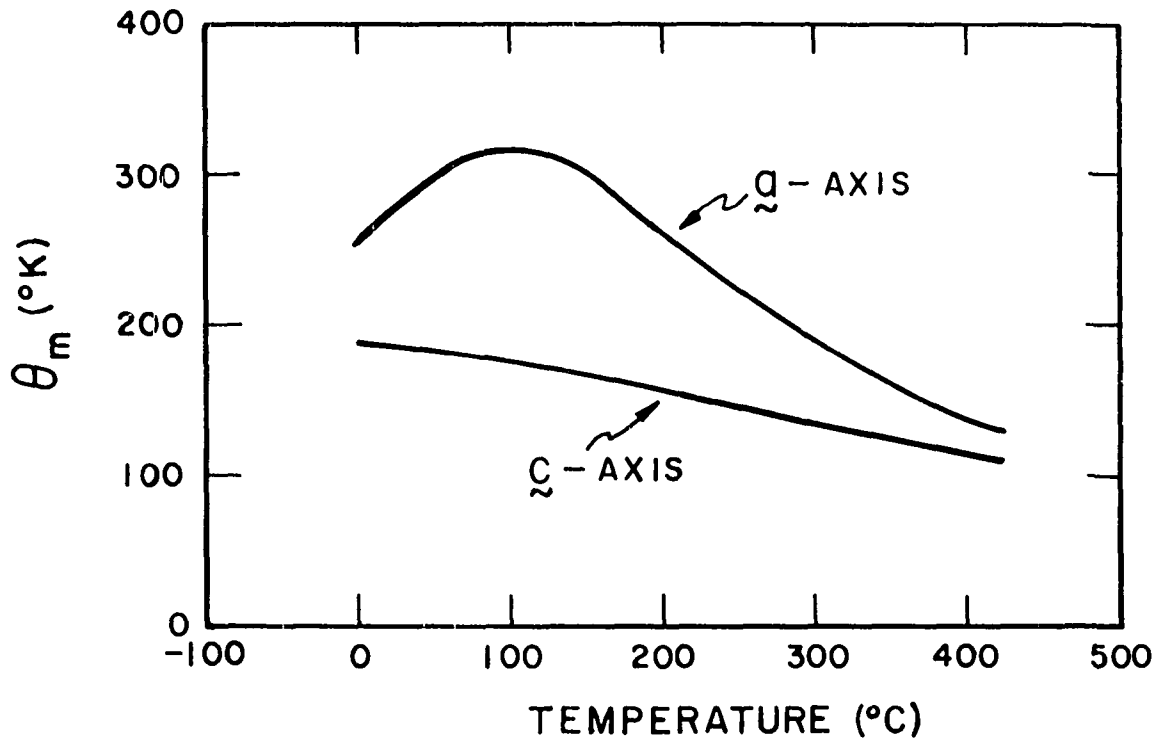

Figure 32. Debye temperature Θ_M versus temperature for zinc for lattice vibrations parallel to the c and a axes

of these calculations is in doubt since the Debye-Waller theory does not adequately explain the behavior of anisotropic metals.

Zener (15) has shown that the equation for the mean square vibration amplitude for any direction in a hexagonal crystal should be of the form:

$$\mu_{\psi}^2 = A \cos^2\psi + B \sin^2\psi, \qquad (43)$$

where ψ is the polar angle between the c axis and the desired direction. Equations 31 and 32 can be substituted in turn into equation 43 to determine A and B. Thus:

$$\mu_{\psi}^2 (T) = \cos^2\psi (15.1085\cdot10^{-19} + 6.4091\cdot10^{-21}T + 1.5388\cdot10^{-24}T^2 + 1.7639\cdot10^{-26}T^3) + \sin^2\psi (5.7295\cdot10^{-19} + 3.1579\cdot10^{-21}T - 1.0610\cdot10^{-23} + 3.4736\cdot10^{-26}T^3) \qquad (44)$$

from which it is possible to calculate the mean square vibration amplitude for any direction in a zinc crystal at any temperature. A plot of this function is shown in Figure 33, which shows the mean square amplitude isotherms at every 100° from 0° to 400°C. Zener calculated a similar function from the velocities of the lattice waves in the solid. His expression for zinc is:

$$\mu_{\psi}^2 (T) = \cos^2\psi (6.83\cdot10^{-19} + 2.50\cdot10^{-21}T) + \sin^2\psi (3.79\cdot10^{-19} + 1.39\cdot10^{-21}T) \qquad (45)$$

where T is in °C. The mean square amplitudes calculated from Zener's equation are much smaller than those obtained in this work. Also, equation 45 exhibits a linear dependence of the mean square amplitude

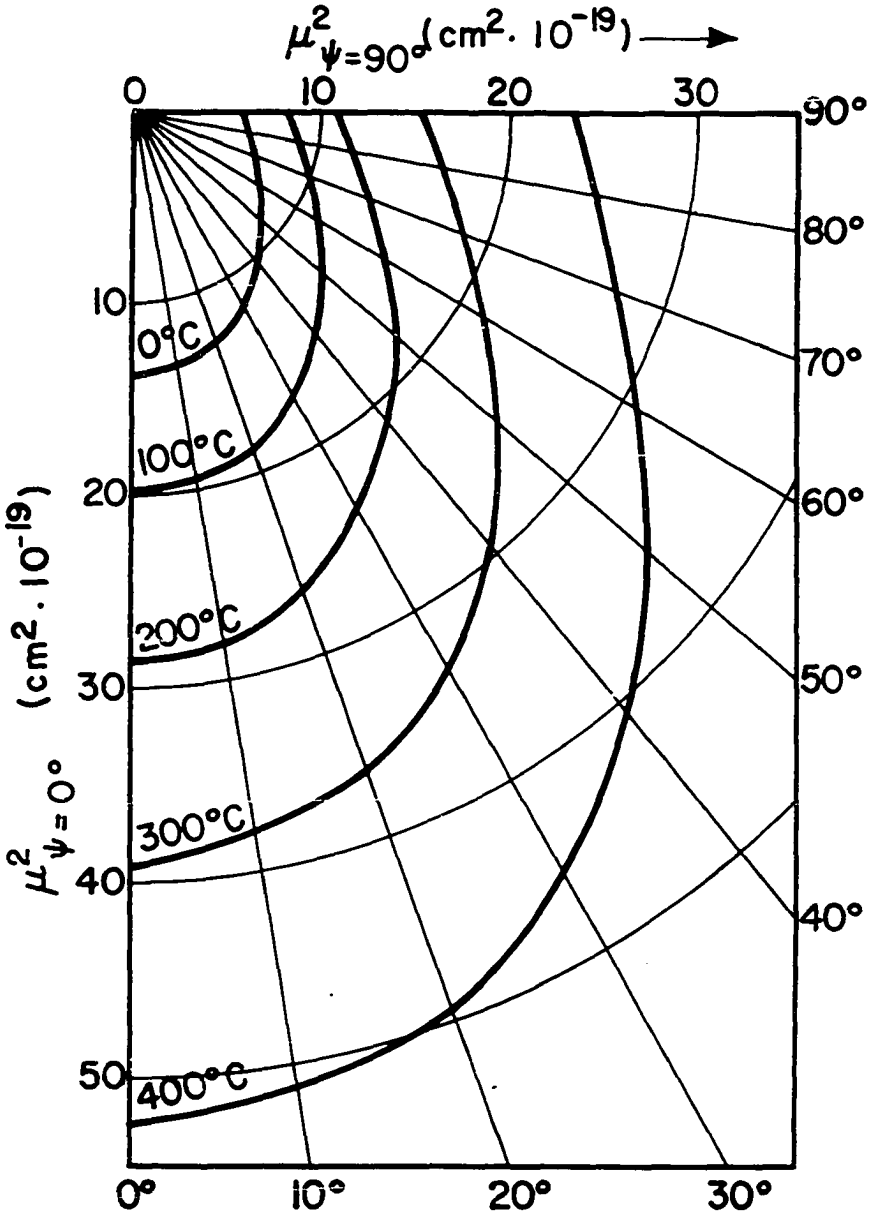

Figure 33. μ^2_ψ (T) isotherms versus polar angle ψ for zinc

on temperature, and the mean square amplitude is zero at T = 0°K.

Jauncey and McNatt (16) and Jauncey and Bruce (17) examined the thermal diffuse scattering from zinc single crystals. They considered that the thermal diffuse scattering appeared as a broad maximum of general scattering, and were able to calculate the mean square vibration amplitudes of the atoms parallel and perpendicular to the major axis. The values they obtained are shown in Table 3, and are plotted in

Table 3. Mean square amplitudes at several temperatures given by Jauncey and McNatt and Jauncey and Bruce

T(°K)	$\mu^2_{\psi=0}$	$\mu^2_{\psi=90}$
100	9.61	2.50
298	29.6	8.65
550	78.4	----

Figure 18. These vibration amplitudes are larger than the values obtained in this work. Even if the intensities were scaled using their values for the mean square amplitudes at 25°C in equation 22, the temperature dependence of the mean square amplitudes obtained in this work does not agree with the temperature dependence indicated by their data, as is evident in Figure 18. This is an indication that the interpretation of the thermal diffuse scattering data by these authors is not strictly correct.

The ratio C between the electrical resistivity and the mean square

vibration amplitude for copper was calculated for temperatures from 0° to 1000°C, using the combined data for all the runs made on the copper single crystal. The resistivity values used were taken from the measurements of Sidles (18) on American Smelting and Refining Company copper of 99.9995% purity. The results are shown in Figure 34. Also shown in Figure 34 are the values of C calculated for this temperature range from the mean square vibration amplitudes calculated from equation 11. The value of C at 0°C is $2.3 \cdot 10^{12}$ ohms/cm. The value of C increases up to about 200°C, and beyond this temperature it has the almost constant value of $2.9 \cdot 10^{12}$ ohms/cm. The theoretical value of C calculated from equation 21 is $2.1 \cdot 10^{12}$ ohms/cm, and this value is only 28% different from the experimental value above 200°C.

Values of the electrical resistivity of zinc as a function of temperature for the directions parallel and perpendicular to the hexagonal $\underset{\sim}{c}$ axis could not be found in the literature. However, the average value for the mean square amplitude given by equation 42 can be compared to the resistivity values for polycrystalline zinc as a function of temperature. A plot of the results are shown in Figure 35. The values of the resistivity from the Handbook of Chemistry and Physics (19) were used to calculate C. It is evident from this plot that the electrical resistivity of zinc is not simply related to the mean square amplitude of vibration of the zinc atoms by a proportionality constant. The values of C range from $6.6 \cdot 10^{12}$ ohms/cm at 0°C to about $4.5 \cdot 10^{12}$ ohms/cm at 400°C, whereas the theoretical value of C calculated from equation 21 is $4.8 \cdot 10^{11}$ ohms/cm.

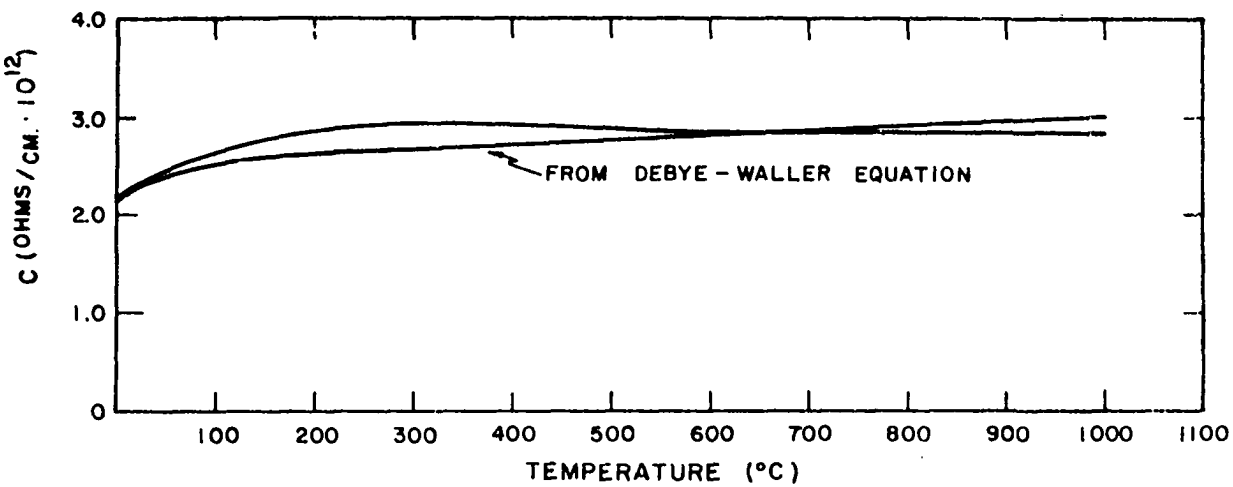

Figure 34. Ratio of the electrical resistivity to the mean square vibration amplitude for copper versus temperature

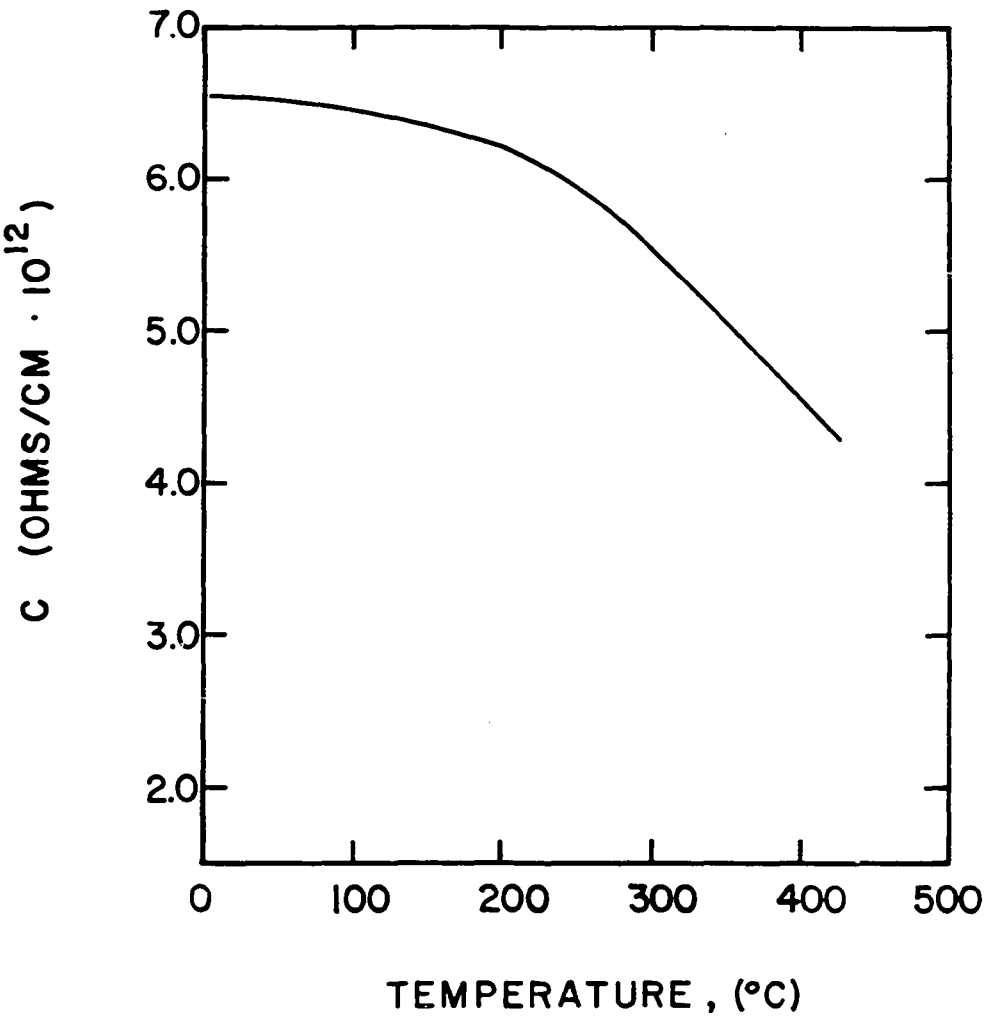

Figure 35. Ratio of the electrical resistivity to the average mean square vibration amplitude for zinc versus temperature

V. SUMMARY

The intensities of x-ray reflections from large single crystals of copper and zinc have been measured as a function of temperature. The (400) reflection for copper and the (0006) and ($2\bar{1}\bar{1}0$) reflections for zinc were examined from 13°C to the melting point of each metal. The data were scaled by calculating a mean square vibration amplitude for the base temperature from the Debye-Waller theory. The mean square amplitudes of vibration as a function of temperature parallel to the $\underset{\sim}{a}$ axis for copper and parallel to the $\underset{\sim}{c}$ and $\underset{\sim}{a}$ axes for zinc were then calculated from the intensity data.

The intensity data were plotted against a reduced temperature defined by the equation:

$$T' = \left(\frac{V(T)}{V(T_o)}\right)^{2\gamma} T$$

For copper, it was found that this plot was linear and thus the Debye-Waller theory when modified by the above expression to correct for the volume expansion of the metal adequately explains the decrease with temperature of the x-ray reflection intensity for copper. For zinc, the plots of the intensity data versus the reduced temperature were not linear, and it is concluded that the modified Debye-Waller theory does not apply to this anisotropic metal.

The mean square vibration amplitudes for copper and zinc were compared to the electrical resistivities as a function of temperature for these metals. The theory of electrical resistivity indicates that the

resistivity is directly proportional to the mean square vibration amplitude. The experimental results for copper confirmed this proportionality for temperatures from 200° to 1000°C, but no correlation was found for zinc when the mean square amplitudes were compared to the resistivity values as a function of temperature for polycrystalline zinc.

Difficulty was experienced in obtaining reproducible intensity measurements. Some evidence is presented which suggests that this difficulty was due to changes in the mosaic structure of the single crystals during thermal cycling.

VI. BIBLIOGRAPHY

1. James, R. W., The Optical Principles of the Diffraction of x-rays, London, G. Bell and Sons, Ltd. (1958).

2. Nilson, N., Arkiv för Fysik, 12, 247 (1957).

3. Young, R. A., X-ray Diffraction Studies of Thermal Motions in Crystals, Georgia Institute of Technology, Engineering Experimental Station, Project A-389, Annual Report No. 1 (1959).

4. Internationale Tabellen zur Bestimmung von Kristallstrukturen. Volume 2. Berlin, Germany, Gebruder Borntraeger (1935).

5. Zener, C. and Bilinsky, S., Physical Review, 50, 101 (1936).

6. Owen, E. A. and Williams, R. W., Proceedings, Royal Society of London, Ser. A, 188, 509 (1947).

7. Paskin, A., Acta Crystallographica, 10, 667 (1957).

8. James, R. W., Brindley, G. W., and Wood, R. G., Proceedings, Royal Society of London, Ser. A, 125, 401 (1929).

9. Boskovits, J., Roilos, M., Theodossiou, A., and Alexopoulos, K., Acta Crystallographica, 11, 845 (1958).

10. Spreadborough, J. and Christian, J. W., Proceedings, Physical Society, London, 74, 609 (1959).

11. Mott, N. F. and Jones, H., The Theory of the Properties of Metals and Alloys, Oxford, England, Clarendon Press (1936).

12. Chiotti, P., Review of Scientific Instruments, 25, 683 (1954).

13. Grüneisen, E. and Goens, E., Zeitschrift für Physik, 29, 141 (1924).

14. Darken, L. S. and Gurry, R. W., Physical Chemistry of Metals, New York, McGraw-Hill Book Company, Inc. (1953).

15. Zener, C., Physical Review, 49, 122 (1936).

16. Jauncey, G. E. M. and McNatt, E. M., Physical Review, 55, 498 (1939).

17. _____ and Bruce, W. A., Physical Review, 51, 1067 (1937).

18. Sidles, P., Values of Electrical Resistivity versus Temperature for Pure Copper (manuscript), Iowa State University of Science and Technology, Institute for Atomic Research, Document Library, Research Notebook No. PS-17 (1958).

19. Handbook of Chemistry and Physics, Cleveland, Ohio, Chemical Publishing Co. (1953).

20. Weisskopf, V. F., American Journal of Physics, 11, 1 (1943).

21. Hamming, R. W. and Weiss, R. A., General Purpose System for the 650: Iρ, File No. 2.0.008, New York, International Business Machines Corporation, IBM Program Library (ca. 1956).

22. Norman, H. L., Matrix Inversion, File No. 5.2.008, New York, International Business Machines Corporation, IBM Program Library (ca. 1957).

VII. ACKNOWLEDGMENTS

The author wishes to express his appreciation to Dr. Premo Chiotti for his guidance and criticisms in this investigation. The author also wishes to acknowledge Dr. Donald E. Williams for instruction in computer programming, and Mr. Bryan G. Lott and Mr. William C. Robinson for their assistance in making the measurements and the necessary calculations.

VIII. APPENDIX A

A. Derivation of the Relation between the Electrical Resistivity and the Mean Square Vibration Amplitude

A classical theoretical treatment can be employed to evaluate the proportionality constant between the electrical resistivity and the mean square vibration amplitudes of the atoms in a metal. The derivation given by Weisskopf (20) will be outlined. For the electrical resistivity:

$$\rho = \frac{2mNv\bar{Q}_d}{ne^2}, \qquad (1)$$

where m is the mass of the electron, e is the charge on the electron, N is the number of atoms per unit volume, n is the number of conduction electrons per unit volume, v is the velocity of the electrons, and $\bar{Q}_d$ is the average scattering cross section of an atom. Weisskopf shows that the ratio of the scattering cross section to the free ion cross section is:

$$\frac{Q_d}{Q_s} = \left[(\underset{\sim}{k} - \underset{\sim}{k}') \cdot \underset{\sim}{d}\right]^2, \qquad (2)$$

where $\underset{\sim}{k}$ is the wave vector of the electron wave before scattering, $\underset{\sim}{k}'$ is the wave vector of the scattered electron wave, and $\underset{\sim}{d}$ is the displacement vector of the atom at the time of scattering. Since the average of the squares of the cosines between $\underset{\sim}{k}$-$\underset{\sim}{k}'$ and $\underset{\sim}{d}$ is 1/3, the average of equation 2 over all the equally probable directions of $\underset{\sim}{d}$ is

$$\frac{Q_d}{Q_s} = \frac{1}{3} \left| \underset{\sim}{k} - \underset{\sim}{k}' \right|^2 \mu^2. \tag{3}$$

Finally, the average of $\left| \underset{\sim}{k} - \underset{\sim}{k}' \right| Q_s$ over all scattering directions, assuming that $\left| \underset{\sim}{k} \right| = \left| \underset{\sim}{k}' \right|$, gives:

$$\bar{Q}_d = \frac{2}{3} k^2 \mu^2 \bar{Q}_s. \tag{4}$$

When equation 4 is substituted into equation 1, the equation:

$$\rho = \frac{4mvk^2 \mu^2 \bar{Q}_s N}{3ne^2} \tag{5}$$

results. Setting $p = mv = \hbar k$ and $p = (2mE)^{1/2}$, equation 5 becomes:

$$\rho = \frac{4(2mE)^{3/2} N \bar{Q}_s}{3\hbar^2 ne^2} \mu^2. \tag{6}$$

Since only electrons having energies near the Fermi level have vacant states into which they can be scattered, E is taken as the Fermi energy, and:

$$C = \frac{4(2mE_F)^{3/2} N \bar{Q}_s}{3\hbar^2 ne^2} \mu^2. \tag{7}$$

IX. APPENDIX B

A. Computer Programs

In order to facilitate the calculations necessary for the interpretation of the data in this study, several programs were written so that these calculations could be performed on an International Business Machine Type 650 computer with punched card input and output. These programs were written using a general purpose routine known as the Bell Lab. II or L_2 language, developed by Hamming and Weiss (21). The advantages of using this language are:

1. Ease of problem formulation; the difficult and often lengthy routines in IBM 650 basic language are avoided.
2. Ease of error decoding; programming errors can in most cases be easily uncovered by "tracing" each step of a calculation controlled by the program.
3. Any changes, additions, or corrections in the program can be effected by adding to and/or removing from the program deck a number of punched cards.

The programs written were designated as LLS, QLS, and DWG, and are described in turn below.

1. LLS. This program constructs a least squares fit of the function:

$$\ln R_{hkl}(T) = \sum_{n=0}^{3} a_n T^n \qquad (1)$$

to the intensity versus temperature data, along with scaling

the intensities, and performing the calculations necessary to obtain the function $\mu^2_{hkl}(T)$. The function:

$$R = \sum_i \left[\ln R_i - \sum_{n=0}^{3} a_n T_i^n \right]^2 \qquad (2)$$

is minimized with respect to the four constants a_n. A solution of four linear simultaneous equations of the form:

$$\sum_i \sum_{n=0}^{3} \left[a_n T_i^{n+j} - T_i^j \ln R_i \right] = 0 , \qquad (3)$$

where $j = 0, 1, 2, 3$ for the four equations, is necessary to obtain the values of the constants. This was effected by using Cramer's rule; the determinants involved were expanded by minors.

2. QIS. This program constructs a least squares fit of the function:

$$d_{hkl} = \sum_{n=0}^{2} b_n T^n \qquad (4)$$

to the interplanar spacing versus temperature data. This function seemed most reasonable from an inspection of the data curves. In this program, the function:

$$R = \sum_i \left[d_i^{hkl} - \sum_{n=0}^{2} b_n T_i^n \right]^2 \qquad (5)$$

is minimized with respect to the three constants b_n. The solution of the three resulting linear simultaneous equations is accomplished by a matrix inversion program developed by Norman (22). This matrix inversion program is used here

because the evaluation of the constants, b_n, is much faster than when Cramer's rule is used, and because the diagonal elements of the inverted matrix can be used to calculate the standard deviations in the constants, according to the relation:

$$\delta b_n = \left[\frac{c^{nn} \sum_{i=1}^{r} (\delta x_i)^2}{r - s} \right]^{1/2} \qquad (6)$$

where δb_n is the standard deviation of b_n, c^{nn} are the diagonal elements of the matrix inverse to the matrix formed by the coefficients of the b_n in the normal equations, δx_i are the deviations of the experimental data from the least squares curve, r is the total number of data points, and s is the number of normal equations.

3. DWΘ. This program evaluates Θ_M in the equation:

$$\ln \frac{R(T_1)}{R(T_2)} = \Gamma^2 (T_m) \left[\frac{3\hbar^2 N_o}{Ak\Theta_M^2(T_m)} (T_2 - T_1) + \gamma\left(\frac{1}{T_2} - \frac{1}{T_1}\right) + \delta\left(\frac{1}{T_2^3} - \frac{1}{T_1^3}\right) \right], \qquad (7)$$

which results directly from a combination of equations 12 and 15. Here, $T_m = \frac{1}{2} |T_1 - T_2|$, A is the atomic weight, and N_o is Avogrado's number. $|T_1 - T_2|$ was chosen as 100°, and a Θ_M was calculated every 25°K. The input data required for program are the constants a_n from the LLS program and the constants b_n from the QLS program.

X. APPENDIX C

Table 4. Integrated intensities, R'_{400}, and Bragg angles, 2θ, as a function of temperature for copper single crystals

Run number	Temperature °C	R'_{400}	2θ degrees
VIII	803	100.5	
	802	100.5	
	679	118	
	677	120	
	588	135.5	
	588	140	
	502	162.5	
	502	166	
	409	187.5	
	406	193	
	301	219.5	
	301	225	
	222.5	232	
	223	227	
	120	256	
	120	255.5	
	13	296.5	
	13	297	
	13	258	
	13	268	
XVa	804	169	114.440
	806	168	114.430
	687	233	114.870
	687	221	114.880
	584	288	115.230
	584	293	115.235
	503	330	115.500
	502	322	115.505
	388	364.5	115.870
	388	378	115.865

Table 4 (continued)

Run number	Temperature °C	R'_{400}	2θ degrees
	388	369	115.870
	389	373	115.880
	288	422	116.180
	288	416	116.180
	204	445	116.430
	13	531	116.965
	13	522	116.965
XVb	14	255	116.965
	14	252	116.960
	14	248	116.965
	121	215	116.665
	121	215	116.665
	209	204	116.425
	210	204.5	116.420
	314	195	116.105
	315	199	116.110
	408	179	115.810
	406	177	115.815
	500	160	115.540
	500	162	115.545
	603	141.5	115.205
	603	147	115.200
	700	125	114.860
	700	119	114.860
	792	100.5	114.575
	792	104	114.565
	900	79	114.170
	898	83	114.165
	1004	69	113.775
	1004	70	113.770
	890	88	114.225
	889	89	114.220
	804	105	114.540
	804	102	114.535
	698	121	114.915
	698	117	114.920
	607	136	115.230

Table 4 (continued)

Run number	Temperature °C	R'_{400}	2θ degrees
	607	130	115.230
	517	151.5	115.530
	515	148.5	115.530
	407	163	115.865
	406	171	115.875
	304	186	116.175
	304	189.5	116.185
	204	207	116.460
	204	202.5	116.460
	115	227	116.690
	115	217	116.695
	14	243	116.955
	14	241	116.965
	14	241	116.965
XVc	14	247	116.960
	14	252	116.955
	108	229	116.715
	108	218	116.715
	202	206	116.460
	202	201	116.460
	290	184	116.210
	290	185	116.210
	405	165	115.865
	403	167	115.875
	490	160	115.620
	490	156	115.615
	579	142	115.340
	579	140	115.340
	679	124	114.990
	679	119	114.970
	784	114	114.635
	784	105	114.640
	908	87.5	114.200
	912	87.5	114.180

Table 4 (continued)

Run number	Temperature °C	R'_{400}	2θ degrees
	1011	71.5	113.820
	1013	77	113.820
	1016	76	113.815
	890	88.5	114.310
	888	88	114.290
	887	86	114.315

Table 5. Integrated intensities, $R'_{000\ell}$, and Bragg angles 2θ, as a function of temperature for zinc single crystal

Run number	Temperature °C	$R'_{000\ell}$	2θ degrees
Xb		R'_{0004}	
	13	221	
	13	223	
	102	181	
	105	178.5	
	191	152	
	191	152	
	303	111	
	305	101	
	399	76	
	399	76	
XIV		R'_{0004}	
	14	247	77.165
	14	250	77.165
	98	195	76.720
	98	191	76.725
	194	163	76.205

Table 5 (continued)

Run number	Temperature °C	R'_{0001}	2θ degrees
	193	157.5	76.235
	303	139	75.680
	304	136	75.680
	410	107	75.190
	408	101	75.200
	323	126	75.585
	318	127	75.605
	216	157	76.110
	215	163	76.115
	106	196.5	76.680
	105	205	76.685
	14	247	77.165
	14	255	77.170
XII		R'_{0006}	
	16	431	
	16	434	
	16	425	
	106	318	
	106	321	
	198	196	
	199	191	
	288	114.5	
	289	109	
	404	41.5	
	404	41	
	303	109	
	208	168	
XIIIa		R'_{0006}	
	391	40	132.455
	388	40	132.490
	275	103	134.160
	275	103	134.165
	198	151	135.350

Table 5 (continued)

Run number	Temperature °C	$R'_{000\ell}$	2θ degrees
	198	150	135.360
	98	249	137.000
	97	250	137.050
	13.5	340	138.510
	13.5	343	138.510
	98	244	137.010
	98	239	137.010
	200	150	135.310
	199	149	135.315
	13	335	138.490
	13	331	138.485
	98	241	137.010
	98	249	137.000
	193	160	135.435
	192	151	135.450
	299	79	133.745
	296	85	133.765
	383	42	132.580
	383	46	132.570
	305.5	72	133.675
	304	75	133.705
	206	131	135.215
	204	135	135.255
	95	231	137.065
	95	219	137.080
	14	315	138.485
XIIIb		R'_{0006}	
	14	293	138.470
	14	286	138.470
	93	212	137.085
	93	209	137.080
	180	153	135.625

Table 5 (continued)

Run number	Temperature °C	$R'_{000\ell}$	2θ degrees
	180	145	135.625
	289	73	133.920
	289	73	133.905
	410	29	132.230
	412	28	132.215
	318	64.5	133.475
	319	59	133.510
	231	110	134.810
	230	108	134.825
	137	174	136.335
	137	173	136.350
	14	290	138.460
	14	291	138.465

Table 6. Integrated intensities, $R'_{2\bar{1}\bar{1}0}$, and Bragg angles, 2θ, as a function of temperature for zinc single crystals

Run number	Temperature °C	$R'_{2\bar{1}\bar{1}0}$	2θ degrees
	14	186	71.090
	14	186	71.090
	116	156.5	70.990
	206	158.5	70.875
	314	156	70.725
	409	130.5	70.550
	403	123	70.550
	308	112	70.720
	219	133.5	70.860
	101	168	71.000
	14	168	71.080
	14	164	71.085
	14	172	71.085
	14	167.5	71.085
	87	170	71.015

Table 6 (continued)

Run number	Temperature °C	$R'_{2\bar{1}\bar{1}0}$	2θ degrees
	197	153	70.885
	290	135	70.745
	396	103	70.560
	396	103	70.565
	288	141	70.755
	288	146	70.755
	188	160	70.890
	187	160	70.895
	103	169.5	70.990
	103	165	71.000
	14	176	71.085
	14	174	71.085
	87	160	71.015
	87	160.5	71.015
	195	152.5	70.885
	195	155	70.885
	301.5	151	70.735
	302	158	70.735
	391	121	70.565
	390.5	129	70.565
	290	159	70.750
	288	154	70.760
	202	170.5	70.875
	202	172	70.875
	101	173	70.995
	101	180	71.000
	14	165	71.090
	14	180	71.085
	14	178	71.085